STRESS ANALYSIS IN OPTICAL SYSTEMS

by

Jeremy Craig Parkinson

A Thesis Submitted to the Faculty of the

JAMES C. WYANT COLLEGE OF OPTICAL SCIENCE

In Partial Fulfillment of the Requirements
For the Degree of

MASTERS OF SCIENCE
WITH A MAJOR IN OPTICAL SCIENCE

In the Graduate College

THE UNIVERSITY OF ARIZONA

2023

THE UNIVERSITY OF ARIZONA
GRADUATE COLLEGE

As members of the Master's Committee, we certify that we have read the thesis prepared by **Jeremy C. Parkinson**, titled ***Stress Analysis in Optical Systems*** and recommend that it be accepted as fulfilling the thesis requirement for the Master's Degree.

_______________________________ Date: 8/11/2023
Professor Meredith K. Kupinski

_______________________________ Date: 8/11/2023
Professor Brandon Chalifoux

_______________________________ Date: 08/11/2023
Professor Gregory Smith

Final approval and acceptance of this thesis is contingent upon the candidate's submission of the final copies of the thesis to the Graduate College.

I hereby certify that I have read this thesis prepared under my direction and recommend that it be accepted as fulfilling the Master's requirement.

_______________________________ Date: 8/11/2023
Professor Meredith K. Kupinski
Master's Thesis Committee Chair
Wyant College of Optical Sciences

STATEMENT BY AUTHOR

SIGNED: ______________________________
Jeremy Craig Parkinson

APPROVAL BY THESIS DIRECTOR

This thesis has been approved on the date shown below:

______________________________ ______________

Put your Thesis Director's name and title into square brackets, [], after the statementbyauthor command Date

ACKNOWLEDGEMENTS

A majority of the work presented here was done in support of a much larger and ongoing effort, which has been made possible only through the support and guidance of many individuals.

Dr. Dong Wu at the NASA Goddard Test Flight Center for enabling and continuing to support the IRCSP project, his expertise and dedication have been instrumental in driving the project's success and advancement.

Dr. Chang Jin Oh and his team at the Optical Engineering and Fabrication Facility within the James C. Wyant College of Optical Science for their guidance and work on the mechanical design and fabrication of the IRCSP instrument enclosure.

I would like to express my heartfelt gratitude to Professor Meredith Kupinski for her invaluable guidance, and support as my graduate advisor. Her expertise, insightful feedback, and patience (a lot of patience...) have been instrumental in shaping the trajectory of both my undergraduate and graduate journey. Her mentorship has not only propelled my academic growth far beyond my own goals, but has also instilled in me a deeper passion for research and experimentation.

DEDICATION

This work is dedicated to my amazing family who have always supported me and encouraged the pursuit of my education.

To my brother Kyle, thank you for pulling me out of my bad habits and securing my first tech-oriented job. I truly do not know where I would be if you were not there for me.

To My brother Evan, watching you pursue your own life goals has been a tremendous source of motivation. I have no doubt that you will accomplish your goals and am extremely proud of you.

To my Mother, whose persistence and strength have been a true inspiration and point of motivation throughout this endeavour. Your love and support have been the most consistent pillars in my life.

And to my father, whose humor and lighthearted attitude towards life continues to guide me through the toughest moments. While you did not get to see this journey completed, you never held the slightest doubt that I would succeed.

I love you all.

LAND ACKNOWLEDGEMENT

We respectfully acknowledge the University of Arizona is on the land and territories of Indigenous peoples. Today, Arizona is home to 22 federally recognized tribes, with Tucson being home to the O'odham and the Yaqui. Committed to diversity and inclusion, the University strives to build sustainable relationships with sovereign Native Nations and Indigenous communities through education offerings, partnerships, and community service.

TABLE OF CONTENTS

TABLE OF CONTENTS – *Continued*

LIST OF FIGURES

LIST OF FIGURES – *Continued*

LIST OF FIGURES – *Continued*

LIST OF TABLES

ABSTRACT

Structural failures can occur when loading conditions cause stress and strain within a material that exceeds the ultimate strength. Similarly, the performance of an optical system can be adversely affected by poorly characterized loading conditions and the resulting stress fields. Rigorous stress analysis is crucial to ensuring a specified performance can be achieved under varying environmental conditions. This work presents stress measurements and analysis for two projects: i) measurement of the stress-optic coefficient of N-Bk7, a glass commonly used for optical components, and ii) a payload design for a high-altitude (≈ 30 [km]) balloon deployment of an Infrared Channeled Spectro-Polarimeter (IRCSP).

The N-Bk7 stress analysis is functionally based on the relationship between stress and measured polarimetric response. Stress in optical systems induces birefringence, where the index of refraction is dependent on the polarization of the incident light. Measuring the retardance of a material can therefore help determine how the stress is affecting the index of refraction of the material. This effect is quantified by the stress optic coefficient. For this work, a Rotating Retarder Mueller Matrix Imaging Polarimeter (RRMIP) was used to measure the linear retardance of a diametrically loaded sample of N-Bk7 at a wavelength of 1550 [nm]. These retardance mea-

surements were used to compute the N-Bk7 stress optic coefficient as compared to industry-reported values.

Prior to the 2021 deployment of IRCSP on a high-altitude balloon, a fully autonomous system was developed to control the image acquisition, focal plane temperature, and humidity of the instrument. Operating this optical system at high altitudes required analysis of the varying environmental conditions to design an instrument enclosure that met both optical and safety specifications. Finite Element Analysis (FEA) was used to show efficacy of the mechanical design under expected flight loads to earn flight approval from Columbia Scientific Balloon Facility (CSBF). This enclosure has been apart of three successful balloon deployments of IRCSP. Additional work to design the electronics for a PID-controlled thermo-electric cooler in also included.

CHAPTER 1

Introduction

1.1 IRCSP Enclosure Design and Deployment

In 2017, a prototype Infrared Channeled Spectro-Polarimeter (IRCSP) was delivered to Goddard Space Flight Center (GSFC) for integration into the Sub-mm Wave and IR Polarimeter (SWIRP) CubeSat while a second clone IRCSP instrument was assembled for laboratory characterization, calibration, and validation. The incident polarization ellipticity is spectrally modulated with a highly dispersive retarder and divided into two paths by a linear polarizer which are then diffracted onto the focal planes [7, 8]. The instrument incorporates two FLIR Boson microbolometers as science cameras. The science objective of the IRCSP is to measure the polarimetric properties of thermal emission from ice particles in clouds. The IRCSP was deployed on a high-altitude balloon during the summer of 2021 as a first flight demonstration. The instrument was installed as a piggyback instrument on Salter Test flight 714NT as part of the 2021 Fort Sumner high-altitude ballooning campaign hosted by NASA Columbia Scientific Balloon Facility (CSBF) [9, 10, 11]. This flight reached an altitude of 33 [km] with minimum ambient temperatures of $-70[^{\circ}C]$ over a duration of 6 hours from launch to landing. An enclosure capable of surviving the conditions of high-altitude flight was needed since the instrument was originally designed for CubeSat integration. A protective enclosure with single board computer and environmental regulation systems was developed for this deployment. An external wide-field camera for context imaging was incorporated into this flight system. SolidWorks was used to to design all parts and assemblies.

The IRCSP was re-deployed in the summer of 2022 onboard a similar high-altitude balloon flight as well as the P3 Orion out of Wallops Flight Facility (WFF). Both CSBF and WFF require structural analysis to show the proposed flight payload can withstand flight conditions. Proper engineering design has all materials operating below their yield stress with acceptable margins as dictated by the required factor of safety. Material properties can change depending on the physical and environmental loading conditions which the structure will be exposed to. All such conditions must be well defined with all selected materials rated to function properly. Thermal loading can lead to length change and changes in a materials response to external forces. Structural elements must not be used below their brittle transition temperature. Acceleration loading must not cause structural elements to experience stresses beyond the acceptable factor of safety. The high altitude flight sees lower temperatures and acceleration loading is more stringent, thus simulations are presented for those worst case conditions. The P3 Orion has the added complexity of significant vibration sources. Modal analysis showed that the resonant frequencies of the IRCSP are sufficiently displaced from the P3 driving frequencies.

1.2 Stress-Optic Coefficient

This work discusses a Mueller matrix imaging experiment to measure the stress optic coefficient, observe the spatial distribution of birefringence, and quantify experimental sources of uncertainty. A one-inch diameter disk of sample material was diametrically loaded with increasing force, and linear retardance was measured in the central region. Stress fields are dependant on loading conditions and component geometries. Closed form mathematical solutions exist for simple cases and with some basic assumption. However, component with complex geometries or assemblies, which combine multiple parts, can have non-linear behaviour and often require complicated numerical methods or approximations which do not hold over large domains. Finite element modeling is a numerical method in which a component in broken down into a collection of discrete nodes, each connected to its neighboring nodes through a localized linear equation. Finite element and analytical modeling was done to estimate the magnitude of stress in this central region. A Rotating Retarder Mueller Matrix Imaging Polarimeter measured the spatial distribution of linear retardance. The retardance is related to the change in birefringence with stress magnitude. The slope of this linear fit is the stress optic coefficient. A 1-inch diameter N-BK7 disk was measured at a wavelength of 1550nm and compared with industry-accepted values. The stress-optic coefficient of N-BK7 was measured as $2.83 \pm 0.1057[TPa]^{-1}$. The published N-BK7 value measured at visible wavelengths is 2.77 $[TPa]^{-1} \pm 3\%$[12, 4, 13]. This agreement validates the experimental Mueller matrix imaging methods and supports the common assumption of minor wavelength dependence of the stress-optic coefficient.

CHAPTER 2

Background

How light interacts with a material is directly dependent on its material properties, which are also tied to the materials' response to stress and strain. To understand light-matter interactions this chapter will introduce relevant characteristics of light and material properties including how they are quantified.

2.1 Material Properties

2.1.1 Refractive index

When light is propagating through vacuum, it moves at the speed of light. When light interacts with molecules and atoms in a non-vacuum medium, the displacement of atoms by the electric and magnetic fields produces resistance and decreases the speed of propagation. The ratio of the velocity of the light inside the medium with that of light in a vacuum gives the refractive index of the medium, $n = c/v$. In addition to dictating the velocity of light in the medium, the refractive index also effects optical properties such as the reflectivity of a surface, the focusing power of a lens, and the optical path length (OPL) of an optical element.

Dispersion is the relationship between refractive index and the frequency of light. In general, some bandwidths have a relatively constant behavior while other spectral regions have a rapidly changing refractive index with discontinuities indicating absorption bands. The Sellmeier equation is an approximation for the wavelength dependence of the refractive index

$$n^2(\lambda) = 1 + \sum_i \frac{B_i \lambda^2}{\lambda^2 - C_i}. \tag{2.1}$$

Cauchy's equation is a simpler approximation with reduced accuracy outside the visible waveband

$$n(\lambda) = A + \frac{B}{\lambda^2} + \frac{C}{\lambda^4} + ... \tag{2.2}$$

Here B_i, C_i in Equation 2.1 and A, B, C in Equation 2.2 are experimentally determined coefficients typically provided by the material manufacturer.

The refractive index can also depend on the polarization state and propagation direction of the light. Such materials are described as being birefringent and induce a phase delay between orthogonal polarization states as each state traverses the material at a different velocity. When light passes through a birefringent material it is split into orthogonal polarizations of varying propagation directions, which experience unique refractive indices, and therefore, an optical path length difference (OPD). The OPD dependence on polarization is referred to as retardance, δ and is reported in degrees, radians, length, or waves. The birefringence, Δn, is the difference in the index of refraction and is, therefore unitless

$$\Delta n = \frac{\delta^\circ}{360^\circ} \frac{\lambda}{t} = \frac{\delta_w \lambda}{t} = \frac{\delta_\lambda}{t}. \tag{2.3}$$

Here t is the material thickness and the linear retardance is shown in varying units:

δ°, δ_w, and δ_λ in units of degrees, waves, and length, respectively.

2.1.2 Isotropy

Crystalline materials, such as quartz or calcite, are characterized by a periodic structure of atoms called a lattice. Asymmetries in the atomic lattice spacing cause the material to adopt up to three unique refractive indices, one for each of the principal axis defining a three-dimensional spatial coordinate system. These anisotropic materials are naturally birefringent and therefore have an optic axis, an orientation in which orthogonal polarization states experience identical indices of refraction. Not to be confused with the optic*al* axis, which is commonly defined as the line connecting the front and rear focal points of an optical system. There is no birefringence when light propagates along the optic axis. A material with two unique indices will be uniaxial with a single optic axis and those with three indices will be biaxial, having two unique optic axes [14, 15, 13].

2.2 Mechanics of Materials

When objects are exposed to external loads, they become stressed. To model this behavior, each element is treated as a spring using Hooke's law. This is an approximation for small elastic deformations which states that deformation of length, Δx, in a material scales linearly with the applied force, F, and a constant, k, refereed to as the stiffness of the material with units of force per unit length

$$F = k\Delta x. \tag{2.4}$$

The inverse of the stiffness is the compliance of the material, $C = 1/k$ and is more common in mechanical analysis. These deformations cause stress and strain in a material. Proper engineering design ensures that stress in a material will remain suitably below their failure points with acceptable margin. The first criterion of interest is a materials' yield strength, or the stress magnitude at which a material transitions from linear, elastic deformation described by Equations 2.4 to plastic. The second criterion is the Ultimate strength, or maximum stress that a material can endure. These two criteria are intrinsic properties of the material and must be analyzed at local points of stress concentrations, areas of structural significance, and individual fasteners. The material strength is experimentally determined and manufacturers will test samples from a batch to ensure it meets the specifications. The design engineer is responsible for ensuring that the as-built material meets the requirements of the design[16, 17].

2.2.1 Stress and Strain

A materials' likelihood of failure for a given loading condition is analyzed through the relationship between the stress, strain, and material properties. At the surface, the external load applies pressure on the object. Pressure is characterized as a force over an area and is expressed in pounds per square inch (psi) or Pascals (Pa), where one Pascal is equivalent to one Newton of force over one square meter, N/m^2. The atoms and molecules on the surface become displaced by the load and thus the pressure is distributed throughout the object. This 3D distribution, or field, is known as stress and is typically denoted as σ in units of pressure. Strain is the ratio of the displacement magnitude with the original length, typically denoted as ε, and is a dimensionless parameter

$$\varepsilon = \frac{\Delta x}{x_0}. \tag{2.5}$$

Plotting the stress versus strain is a common method of analyzing a materials' mechanical performance, known as the stress-strain curve [1, 16, 17, 15, 13].

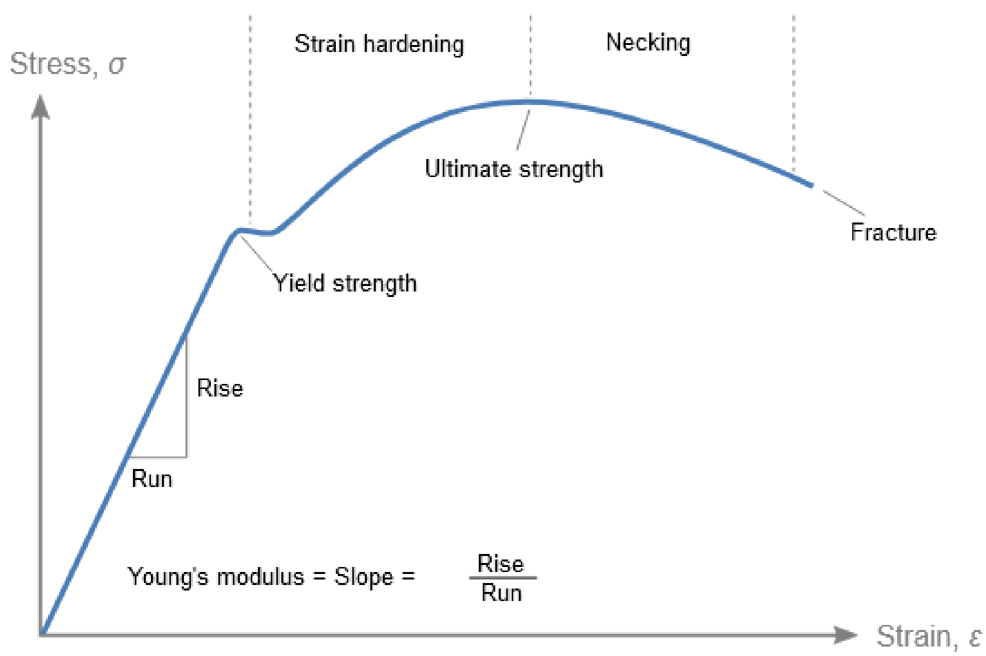

Figure 2.1 Stress strain curve for ductile materials showing the key properties. Deformations are elastic prior to the Yield stress when the transition to plastic behavior. The ultimate stress is the maximum stress a material will experience. Image credit Wikipedia [1].

For small stresses in which Hooke's law holds, the slope of the stress-strain curve defines the Young's modulus, E, which quantifies the stiffness of a material. In this region, the material is said to be experiencing linear elastic deformation, where the material will return to its original shape when the loading is released

$$E = \frac{\sigma}{\varepsilon} = \frac{kx_0}{A}. \tag{2.6}$$

A material with a low Young's modulus, e.g. aluminum or lead, is said to be ductile and will transition between temporary, elastic, and permanent, plastic, deformation when loaded. A high modulus is characteristic of brittle materials, such as glass and ceramics, which will display minimal elastic deformation before fracturing with no plastic deformation. The Young's modulus is dependent on temperature and some materials can transition from ductile to brittle behavior when cooled below a certain temperature, creatively referred to as the ductile-to-brittle transition temperature. Therefore, a mechanical analysis at the most extreme operating conditions must consider the proper regime of the stress-strain relationship in Figure 2.1.

The linear approximation breaks down when the stress in a material passes the yield strength. At this magnitude of stress, the material transitions to plastic deformation as the stress approaches the ultimate strength. When a material is plastically deformed, the atomic bonds in the material begin to break and form a new, permanent structure. Plastically deformed materials will not return to their original state when loading is released. No element of a system should be designed to operate past its yield strength, an engineer must ensure that maximum loading conditions are below the yield strength with suitable margin of safety.

Cauchy Stress Tensor

Nine components define the state of stress at a point inside a material. Each point is characterized as the intersection between three planes with each plane having three stress components: one normal stress and two shear stress components. Normal stresses are denoted as σ_i where i denotes a basis vector of a coordinate system, (e.g. $\widehat{\mathbf{x}}$, $\widehat{\mathbf{y}}$, or $\widehat{\mathbf{z}}$). The two shear stresses are denoted as τ_{ij} where i is the same basis dimension as the normal component with j being one of the two orthogonal dimensions, and therefore represent the components which remain in the $i-j$ plane. For example, the xy-plane will have normal stress in the z-direction, σ_z, with shear stresses in the x and y directions, τ_{zx} and τ_{zy} respectively. Figure 2.2 shows the 3-dimensional stress element with the three planes constructing a three-dimensional coordinate system. The stresses at a given point in a material are denoted, $\boldsymbol{\sigma}$, the Cauchy stress tensor. This tensor reduces to a symmetric matrix for 3D stress fields

$$\boldsymbol{\sigma} = \begin{bmatrix} \sigma_x & \tau_{xy} & \tau_{xz} \\ \tau_{yx} & \sigma_y & \tau_{yz} \\ \tau_{zx} & \tau_{zy} & \sigma_z \end{bmatrix} \equiv \begin{bmatrix} \sigma_x & \tau_{xy} & \tau_{xz} \\ \tau_{xy} & \sigma_y & \tau_{yz} \\ \tau_{xz} & \tau_{yz} & \sigma_z \end{bmatrix}. \tag{2.7}$$

Depending on the loading conditions and component geometry, the stress field may be well approximated as a two-dimensional plane. This plane-stress approximation is valid when the stress in one dimension is decoupled from the two orthogonal

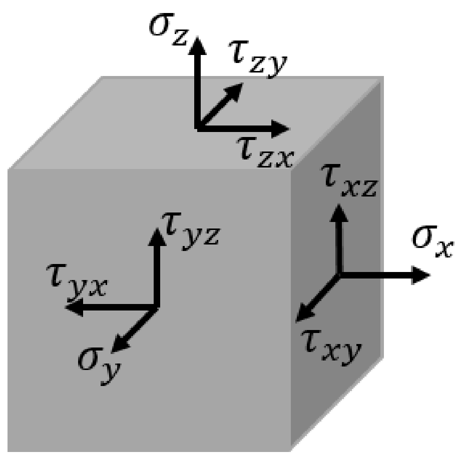

Figure 2.2 The Cauchy stress tensor is formed from the normal and sheer stress components for each plane of a differential volume element.

dimensions. Such conditions arise when one dimension is much less than the orthogonal dimensions or when a loading force is even distributed along one dimension. The diametrically loaded thin disk is one such case. The stress element depicted in Figure 2.2 is simplified to the two-dimensional plane as depicted in Figure 2.3.

$$\boldsymbol{\sigma} = \begin{bmatrix} \sigma_x & \tau_{xy} & \tau_{xz} \\ \tau_{xy} & \sigma_y & \tau_{yz} \\ \tau_{xz} & \tau_{yz} & \sigma_z \end{bmatrix} \rightarrow \begin{bmatrix} \sigma_x & \tau_{xy} \\ \tau_{xy} & \sigma_y \end{bmatrix} \tag{2.8}$$

The principal stress components are calculated from the normal and shear stress values

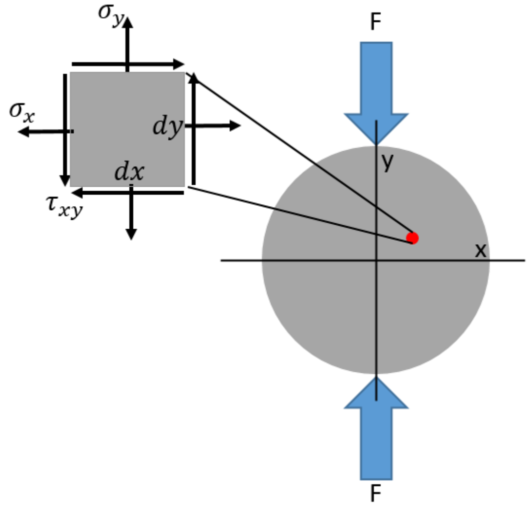

Figure 2.3 The stress at each point is determined by the stress element with differential area.

$$\sigma_{1/2} = \frac{\sigma_x + \sigma_y}{2} \pm \sqrt{\left(\frac{\sigma_x - \sigma_y}{2}\right)^2 + \tau_{xy}^2} \ . \tag{2.9}$$

Here σ_1 is the orientation of maximum stress and σ_2 is the minimum. Outside the plane-stress approximation a third, intermediate magnitude, principal stress component can be derived. Diagonalization of $\boldsymbol{\sigma}$ can be used to derive all three principal stresses for the three-dimensional case. The orientation of σ_1 is denoted as θ_p given by

$$\theta_p = \arctan\left(\frac{2\tau_{xy}}{\sigma_x - \sigma_y}\right). \tag{2.10}$$

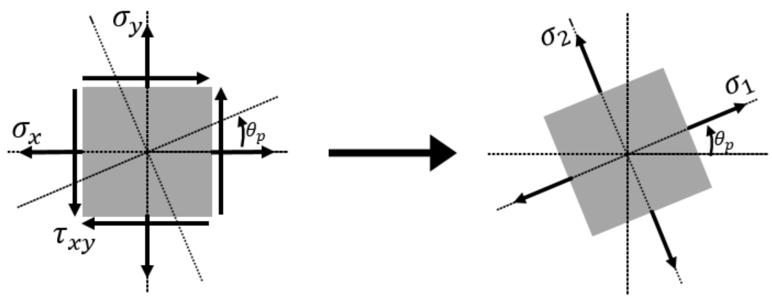

Figure 2.4 The primary principle stresses for each stress element are the maximum, σ_1 and minimum σ_2 stress values.

2.2.2 Von Mises Yield Criterion

Material failure is not often the result of one single stress component but rather a net result of all six unique stress elements. For ductile materials, The Von Mises yield criterion is a scalar stress value that is used to determine failure. The Von Mises stress is calculated from all six components of the Cauchy stress tensor

$$\sigma_v = \frac{1}{\sqrt{2}}\sqrt{(\sigma_x - \sigma_y)^2 + (\sigma_y - \sigma_z)^2 + (\sigma_z - \sigma_x)^2 + 6\left(\tau_{xy}^2 + \tau_{yz}^2 + \tau_{zx}^2\right)}. \qquad (2.11)$$

The Von Mises stress can also be calculated from the principal stresses

$$\sigma_v = \frac{1}{\sqrt{2}}\sqrt{(\sigma_1 - \sigma_2)^2 + (\sigma_2 - \sigma_3)^2 + (\sigma_3 - \sigma_1)^2}. \qquad (2.12)$$

2.2.3 Factor of Safety

With all the assumptions and approximations that go into modeling stress fields, engineering an element to balance at the edge of its elastic region is not acceptable. Furthermore, the as-built material may achieve lower strength than specified or rare weather events may push the environment outside expected conditions. To account for these unknown, and other unknowable, parameters, appropriate margins should be specified between the maximum expected Von Mises stress and the yield strength. A factor of safety, FS, is used to place a limit on the maximum allowable value of σ_v. The FS is the ratio of the yield strength, or the ultimate strength, to the maximum allowable Von Mises stress, $\sigma_{v_{allow}}$. Safety Factors are often a design requirement dictated by laws and regulatory agencies and provided well in advance to any design or analysis is preformed [17, 18, 19, 6, 16]. The yield stress factor of safety is used in conjunction with the yield strength to give to give the maximum allowable stress

$$\sigma_{v_{allow}} = \frac{\sigma_{yield}}{FS_{yield}}. \tag{2.13}$$

The safety factor is defined independently for the yield stress, FS_y, and the Ultimate safety factor FS_u. Safety factors are strictly greater than one and can be as high as 12 or more, meaning that the yield strength must be 12 times greater than the maximum expected stress. Complex structures with poorly understood loading conditions and those which pose significant risks to human safety typically have higher required safety factors. However, a high safety factor requires more reinforcement and therefore a heavier, more expensive, system, which may not be feasible. Aerospace vehicles for example, have safety factors between 1.2 and 2.5 as they have significant weight constraints. Such requirements put added importance on accurate modeling and precision design. The margin of safety then quantifies how far below the respective strength parameter the maximum expected stress is. The margin of safety is strictly greater than zero with no upper bound

$$MS_y = \frac{\sigma_{yield}}{FS_{yield}P} - 1 \tag{2.14}$$

and

$$MS_U = \frac{\sigma_{Ultimate}}{FS_{Ultimate}P} - 1. \tag{2.15}$$

2.3 Photo Elasticity

Isotropic materials can be made anisotropic through the application of external forces. Strain in the atomic lattice alters the refractive index; this phenomenon is known as the photo-elastic effect. Stress from external forces causes deformations in the atomic arrangement of the material. The ratio of these deformations to the original size of the element is known as strain. This strain causes a discernible birefringence to be induced depending upon the materials' properties. The induced optic axis is along the line of action of the applied force. Therefore, any light that is not propagating co-linearly with the line of action will experience retardance. The stress optic coefficient is the linear relation between the magnitude of induced birefringence and applied force. Therefore, a materials' stress-optic coefficient is useful for anticipating a materials' optical properties in various mechanical and thermal operating environments [20, 14, 21, 13, 22, 23].

$$\Delta n = C(\sigma_1 - \sigma_2) \tag{2.16}$$

where C is the relative stress-optic coefficient is units of inverse pressure. There are two stress optic coefficients, one for each of the two principal indices, n_x and n_y. These two coefficients are summed to form the relative stress optic coefficient, simplifying the model for total OPD. For many common optical materials, the relative stress optic coefficient is on the order of $10^{-12}Pa^{-1}$ and reported in units of inverse Tera-Pascals $[TPa]^{-1}$. Compressive stress causes the refractive index to increase and thus results in slower propagation rates while tensile stress has the opposite effect. Stress-induced birefringence is commonly modeled as a purely linear retarder. As light is a transverse wave, any change in the refractive index oriented co-linearly with the direction or propagation has no affect on the OPD and thus has no contributions to net retardance. The plane-stress approximation is therefore well suited for modeling stress birefringence. [20, 14, 24, 13, 25, 26, 22].

2.4 Finite Element Modeling

Mechanical and thermal analysis can become complex as the geometry of a part or system grows more intricate and when multiple loading forces must be incorporated. In many cases, a closed form analytical solution for the stress field simply does not exists. The equations can be simplified from their differential form into a system of linear equations through the Runge–Kutta method. Each equation is decomposed into a discrete form and treated as recursive, where a given value is determined from the value before. The Finite element method adapts the Runge-Kutta approach into two and three dimensional stress field by dividing a continuous material into a finite number of element connected through a simple mesh geometry. Computer aided design (CAD) software such as SolidWorks, Ansys, and Creo, incorporate simulation software built upon the finite element approach.

CHAPTER 3

Enclosure Design

3.1 Introduction

Figure 3.1 The 2021 IRCSP enclosure mounted to the Salter Test Flight gondola pre-launch. The instrument is encased in 1″ polystyrene insulation and several layers of aluminized Mylar film.

The IRCSP was deployed on a high-altitude balloon during the summer of 2021 as a first flight demonstration. This flight reached an altitude of $33[km]$ with minimum ambient temperatures of $-70[°C]$ over a duration of six hours from launch to landing. An enclosure capable of surviving the conditions of high-altitude flight was needed since the instrument was originally designed for CubeSat integration. The main concerns are extremely low temperatures, rapid temperature swings, and condensation on the infrared optics. Furthermore, a battery-operated autonomous control system was needed to operate the instrument. A protective enclosure with a single board computer and environmental regulation systems was developed for this deployment.

The 2021 iteration was a simple enclosure designed to house the original CubeSat instrument and provide basic controls and minimal environmental management. Pressure was not regulated. Two intentional leakage paths were installed with one-way check valves. Passive humidity control was achieved through a chamber filled with Drierite^{TM} on the pressure inlet path as well as silica gel desiccant packs interior to the enclosure. The success of the 2021 flight warranted pursuit of further deployment opportunities. In 2022, the instrument was flown on a similar high-altitude balloon out of Fort Sumner, New Mexico as well as onboard a P-3B Orion (N426NA) Airborne Laboratory out of Wallops Flight Facility (WFF). These flight opportunities enabled further development of the flight enclosure to include:

- Pressure vessel with dry nitrogen environment.
- Context imaging camera.
- Additional environmental sensors.
- Improved thermal regulation of science cameras.

Unfortunately, neither of these two 2022 deployments yielded usable data. The high-altitude balloon flight experienced a software glitch soon after take-off which

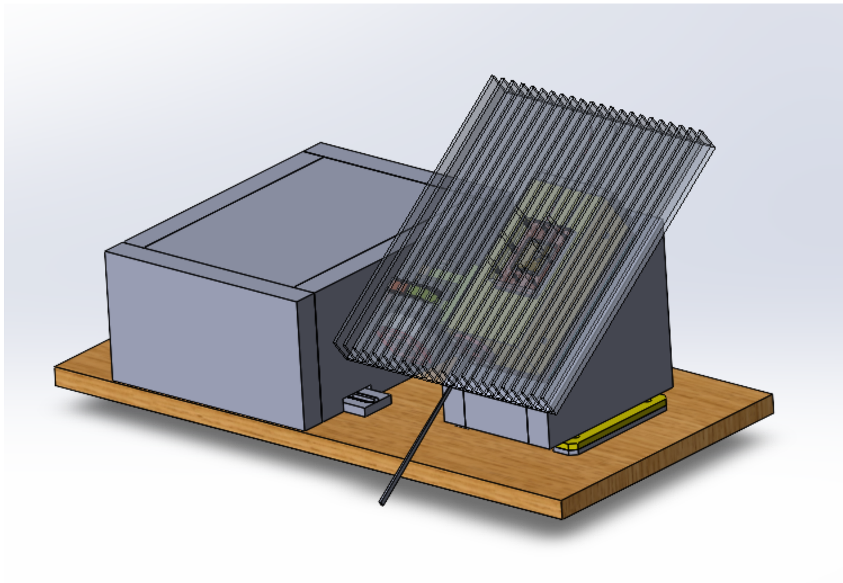

Figure 3.2 The 2023 IRCSP enclosure with context camera and large area radiator. The instrument will be encased in 1-inch polystyrene insulation and several layers of aluminized Mylar film.

prevented data collection. The P3-Orion flight consisted of several downward spirals and subsequent ascents. The instrument was located in the enclosed bomb-bay which is not climate controlled. Therefore, the air temperature inside the compartment fluctuated with the rapidly changing ambient temperatures. Additionally, the compartment has no air flow to facilitate forced convection and radiative cooling is coupled to the aircraft fuselage and therefore diminished. The remaining natural convection was not sufficient to maintain a stable temperature resulting in rapid temperature fluctuations of the IRCSP.

3.2 Requirements

Basic functionality of the instrument on the high-altitude balloon platform was demonstrated in 2021 [9, 10, 8]. For this mission to be a success, the IRCSP needed to acquire at least one frame of data at float altitude and return, intact, to the surface. Survivability requirements are dictated almost exclusively by the two science cameras on board the IRCSP. Atmospheric conditions such as temperature, pressure, and density were modeled using the U.S. Standard Atmosphere [27, 28]. The primary design consideration are:

- The FLIR microbolometers are sensitive to temperature fluctuations and have a minimum survivable temperature of $-40[^{\circ}C]$ [29].
- Water is strongly absorptive in the thermal IR bandwidth which the IRCSP is designed to operate.
- CSBF provides batteries capable of operating at high altitude which provide 900 [Wh] of power at 30[V] and 30[Ah].
- NASA's Gondola Structural Design specifications require a safety review process for piggyback mission fight approval.

Ambient temperatures are modeled to be as low as $-70[^{\circ}C]$. The cameras put out a combined power of, at most, $5[W]$ which is not sufficient to keep the instrument suitably above ambient conditions. Therefore, the IRCSP must be insulated to dampen the influence of ambient conditions on the temperature of the instrument. Furthermore, temperature stability is of critical importance as the bolometer's bias voltage is dependent on the focal plane temperature and rapid temperature fluctuations will invalidate the calibration [9, 10]. These combined factors require an active cooling solution to slow and stabilize the instrument temperature. Water vapour and potential condensation then pose a second environmental concern. These conditions have flowed into engineering requirements for the design of the enclosure.

1. The temperature of the IRCSP shall not fall below $-35[°C]$

   1.1 The IRCSP should achieve a stable temperature at float altitude.

   1.2 The IRCSP may achieve a stable temperature of minus $-30 \pm 1[°C]$ at float altitude.

2. The IRCSP shall achieve a minimum altitude of 15 km.

3. The IRCSP shall be hermetically sealed.

4. The IRCSP shall be dehumidified to $\leq 1.0\%$ relative humidity at $20[°C]$.

   4.1 The IRCSP should be purged with nitrogen.

5. The IRCSP shall acquire one frame of data at float altitude.

   5.1 The IRCSP should acquire data for at least three hours at float altitude.

   5.2 The IRCSP may acquire data during ascent and descent periods.

3.3 Payload Systems

The IRCSP payload is comprised of three major components: the IRCSP instrument enclosure, mounting structure for the instrument enclosure, and an electronics box as shown in Figure 3.2. While the electronics box is a simple aluminum enclosure housing the flight computer and environmental regulation systems, the IRCSP enclosure was carefully designed to ensure the survivability of the instrument. The instrument enclosure encompasses the mounting structure for a wide field thermal imaging camera for scene context and a large area radiator for thermal management. The enclosure is hermetically sealed and therefore requires pressure testing as the ambient pressure will approach zero at float altitude.

3.4 Mechanical design

CSBF has a required yield stress factor of safety $FS_y = 1.25$ and $FS_u = 1.4$ on all flight hardware as outlined in [5]. The IRCSP mounting components have a margin of safety > 0 for MS_y and MS_u which meets the respective safety factor for the required loading conditions. Pressure systems must meet specifications set by ANSI/AIAA S-080A-2018 Space Systems—Metallic Pressure Vessels, Pressurized Structures, and Pressure Components [6]. Loading conditions required by CSBF are presented in Table 3.1 and pressure vessel requirements are presented in Table 3.4

The margin of safety was computed from finite element analysis in SolidWorks. Component contacts were treated as bonded. Remote masses are placed at the

Loading condition	Acceleration
Horizontal	4g
45°	4g
Vertical	8g

Table 3.1 Requested loading conditions for stress analysis from 820-pg-8700.0.1 gondola structural design requirements [5].

center of mass for the respective assembly and affixed to the appropriate fastening locations. Stress on fasteners is calculated independently for pure shear and normal forces.

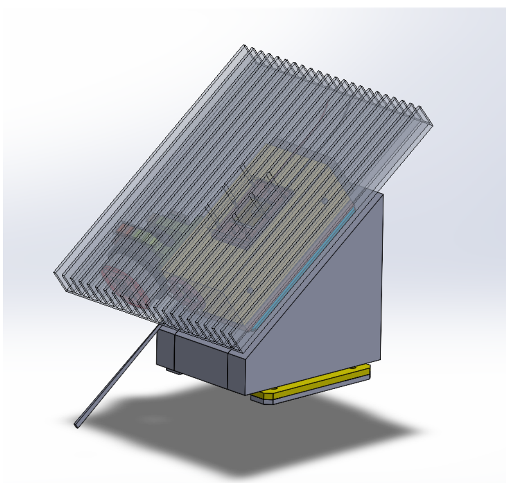

(a) Isometric View of IRCSP with radiator

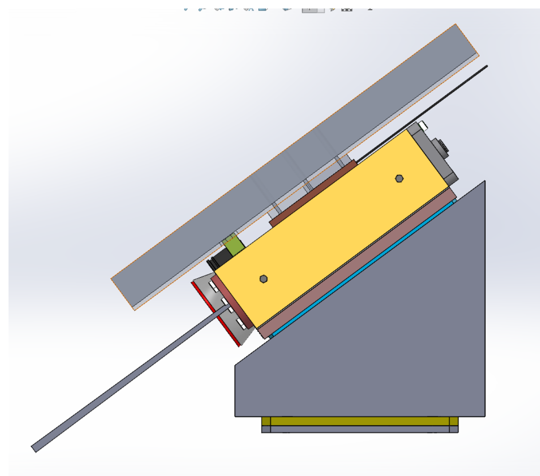

(b) Side View of IRCSP with radiator

Figure 3.3 The 2023 balloon system isolated to the mounting structure requiring safety analysis to ensure acceptable margin of safety on flight stress. This model incorporates a physical representation of the 0.4° HFOV of the IRCSP.

3.4.1 Mounting Brackets

The mounting brackets of the IRCSP payload are fabricated from 6061 Aluminum. The ultimate tensile stress, $\sigma_{u_{AL}}$, for 6061 Aluminum is $45[ksi]$ and the yield

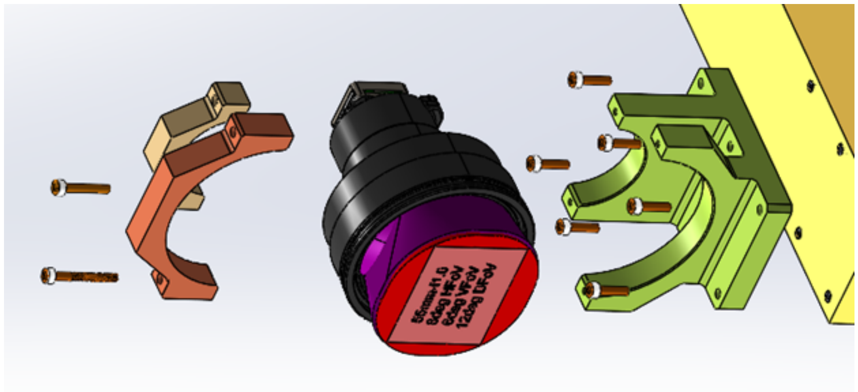

Figure 3.4 Exploded diagram for the context camera mounted to the side of the instrument. Six M3 screws are attached to the enclosure with two M2 screws securing each of the two clamps holding the camera in place.

strength, $\sigma_{y_{AL}}$, is 35 [ksi]. To model the structure under requested loading condition, the instrument enclosure is modeled as a remote mass affixed to the mounting brackets at the bolt locations as shown in Figure 3.5. The context camera was treated similarly with a remote mass distributed along the contact area, see Figure 3.6. The simulation was run under gravitational loading conditions provided by CSBF presented in Table 3.1.

Component	Worst Case Loading condition	flight Stress [psi]	MS_y	MS_u
IRCSP Mount	8g Nadir	2501	10.20	11.00
Context Camera	8g Nadir	26200	0.07	0.15

Table 3.2 Table of simulations results showing acceptable margin of safety for each of the loading conditions. The context camera Von Mises stress is saturated by the pre-load stress form the foundation bolts.

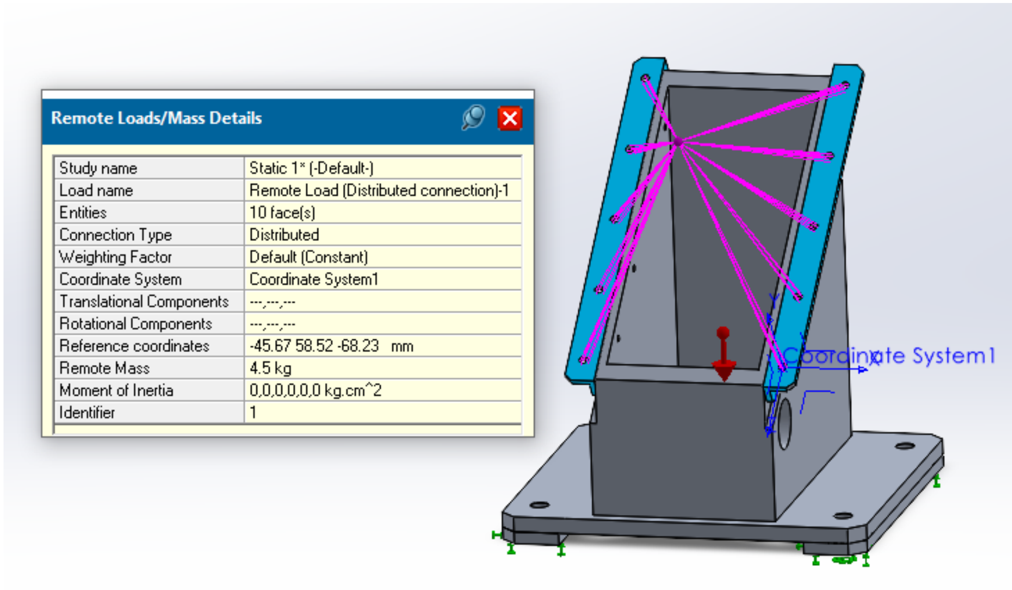

Figure 3.5 Finite Element model with remote mass affixed to bolt pattern and gravitational acceleration acting in the nadir direction.

3.4.2 Fastener Analysis

The fasteners which pose structural significance are securing: IRCSP and balloon gondola, housing and the mount, context camera and the housing, and the large area radiator to the IRCSP. The IRCSP mount is fixtured to the gondola with 1/4-20 A286 SS Socket Head Cap screws. The IRCSP Housing is connected to the Mount with ten M2.5-0.45 x 8 $[mm]$ screws. The radiator is attached to the enclosure with eight M2 x 20 $[mm]$ 18-8 Stainless Steel Socket Head Screws.

The pre-load torque specification under dry conditions for these screws was pulled from 540-PG-8072.1.2B Mechanical Fastener Torque Guidelines as depicted in Figure 3.9. The methods used to calculate preload stress of each fastener are also

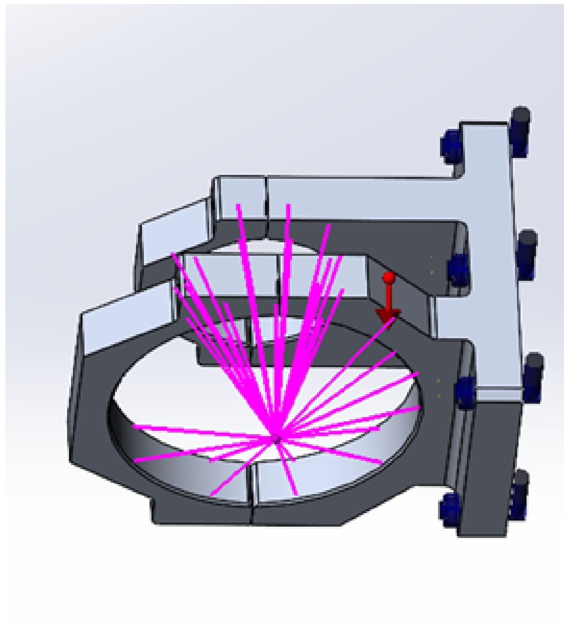

Figure 3.6 Finite element model for the context camera with remote mass distributed on the contact surface. M3 foundation bolts attach this bracket to a virtual wall.

outlined in Section E of Appendix A of 540-PG-8072.1.2B [2].

The screws are modeled in SolidWorks with the AISI 304 stainless steel material from the default SolidWorks library. The ultimate stress, $\sigma_{u_{304}}$, for 304 stainless steel is $75[ksi]$ and the yield strength, $\sigma_{y_{304}}$, is $30[ksi]$. The IRCSP is tilted at a 53.5° with respect to nadir. This tilt, and cosine reduction of any applied force, is ignored in the stress analysis to give a worst-case scenario.

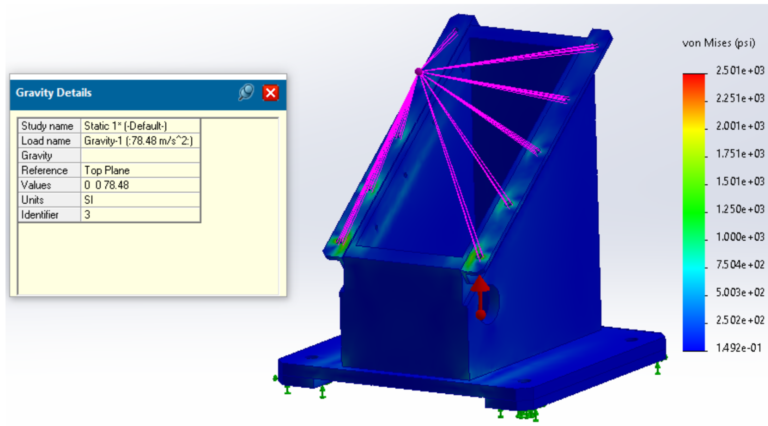

(a) Acceleration loading of 8g's in both zenith and nadir directions produces a maximum Von Mises stress of 2501 [psi].

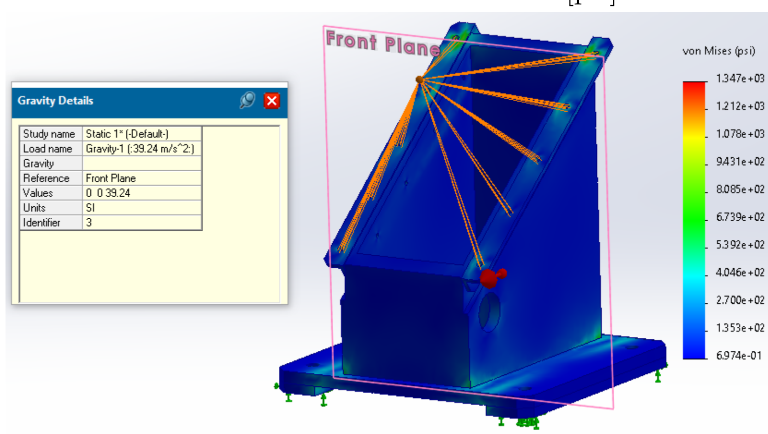

(b) Acceleration loading of 4g's in both forward and reverse directions produces a maximum Von Mises stress of 1347 [psi].

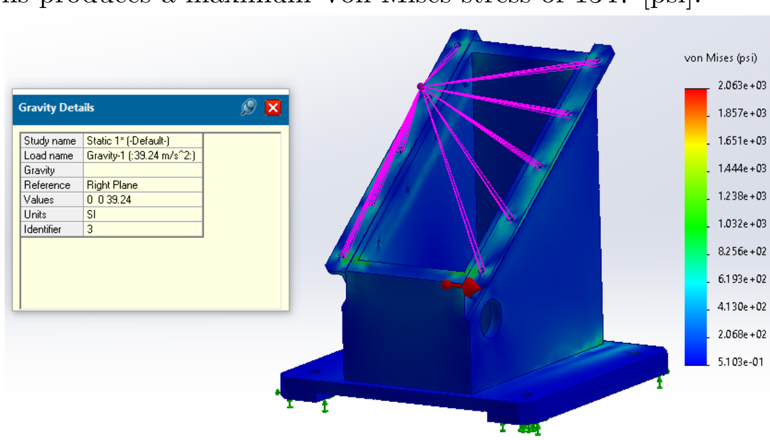

(c) Acceleration loading of 4g's in both lateral left and right directions produces a maximum Von Mises stress of 2063 [psi].

Figure 3.7 Finite Element Modeling of the IRCSP flight mount. The simulation was run at $\pm 8g's$ in vertical and $\pm 4g's$ in horizontal.

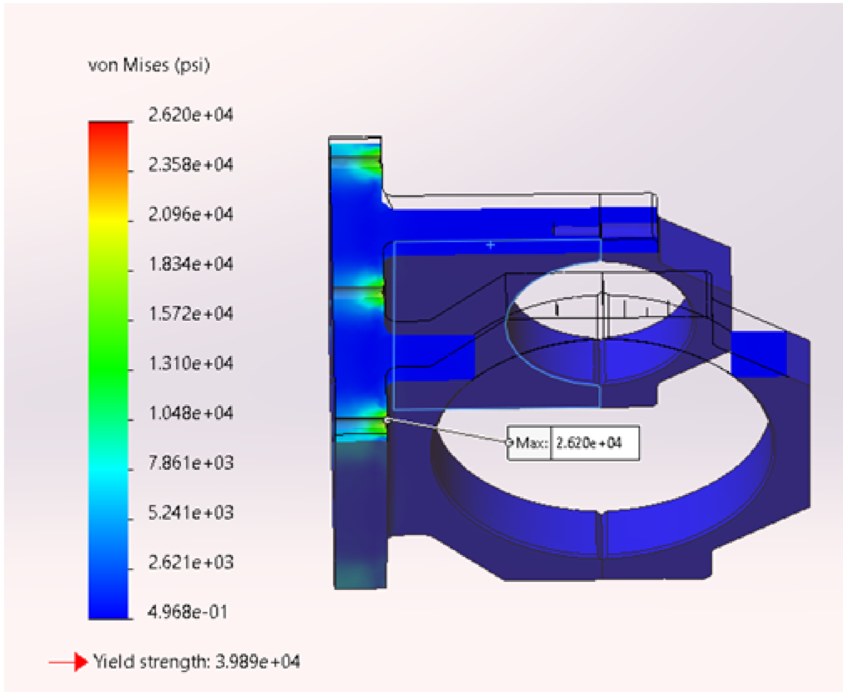

Figure 3.8 FEA results for the context camera mount. The maximum stress occurs at the bolt location and is resulting from the pre-load torque on the bolts.

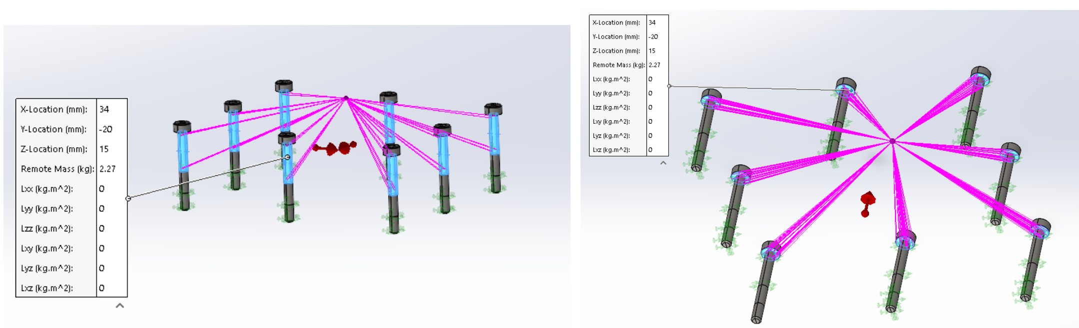

(a) Remote mass attached to screw walls. (b) Remote mass attached screw heads

Figure 3.11 A remote mass of $2.27[kg]$ was located at the center of mass of the radiator with respect to the bolt pattern. The mass was attached to the screw walls for the shear loading forces and then attached to the base of the screw heads for the vertical loading.

DIRECTIVE NO.	540-PG-8072.1.2B	Page 22 of 30
EFFECTIVE DATE:	July 7, 2020	
EXPIRATION DATE:	July 7, 2025	

Table 3-4 Material: A286 Ftu = 160 Ksi Fty = 120 Ksi

		Dry Ultrasonically Cleaned (K=0.30)		Lubricated (K=0.18)		Arathane (K=0.22)	
Fastener Size	Preload (lbs)	Target Torque (in-lb)	Target Torque (ft-lb)	Target Torque (in-lb)	Target Torque (ft-lb)	Target Torque (in-lb)	Target Torque (ft-lb)
#0-80	156	2.8		1.7		2.1	
# 2-56	312	8.0		4.8		5.9	
# 4-40	468	15.7		9.4		11.5	
# 6-32	702	29		17		21	
# 8-32	1092	54		32		39	
#10-24	1404	80		48		59	
#10-32	1560	89	7	53	4	65	5
1/4-20	2496	187	16	112	9	137	11
1/4-28	2808	211	18	126	11	154	13
5/16-18	4134	388	32	233	19	285	24

Figure 3.9 Table 3-4 of 540-PG-8072.1.2B[2] showing target torque for various screw sizes.

Load direction	Acceleration	flight Stress [psi]	MS_y	MS_u
Horizontal	4g	5490	4.37	3.91
Horizontal	8g	10950	2.19	1.96
Zenith	8g	2410	9.96	8.89

Table 3.3 Table of simulations results showing acceptable margin of safety for each of the loading conditions applied to the screws securing the large area radiator.

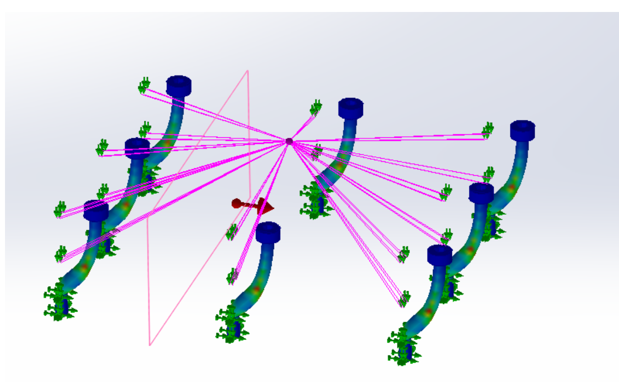

Figure 3.12 The exaggerated deformation results of loading the screws with a pure shear loading.

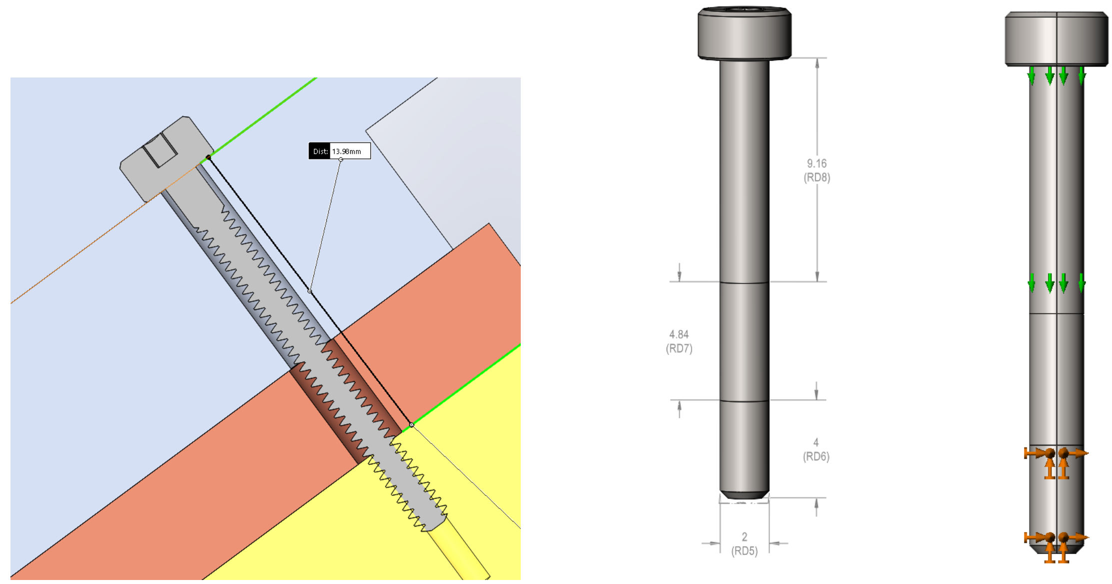

(a) Closeup of one screw used to attach the radiator

(b) dimensions in millimeters

(c) Fixturing for each screw

Figure 3.10 The screws used to secure the radiator are M2 x 18 [mm]. The through hole on the radiator is 9.16[mm] deep. The screws clamp the radiator to the IRCSP with a G10 fiberglass spacer to prevent stress on the ceramic thermo-electric cooler while also preventing thermal conduction. The G10 spacer is 4.84 [mm] thick and the bolts penetrate 4.0[mm] into the threaded holes of the housing. The 4.0[mm] section is treated as fixed geometry and the 9.16[mm] section has a roller fixture allowing transnational motion but no tip/tilt movement.

3.4.3 Hermetic Seal

The science cameras on the IRCSP are officially rated to survive pressures as low as 19[kPa], equal to atmospheric pressure at an altitude of 12 [km] [29]. The Aluminum enclosure was simulated in SolidWorks to determine the maximum Von Mises stress under expected pressure loading of 15[psi] as shown in Figure 3.14. The maximum observed stress was 707.2[psi] producing a $MS_y = 35.3$ and $MS_u = 41.4$.

Component	Minimum Burst Factor (BF)	Proof Factor	Negative Pressure Factor	Minimum Design Safety Factor (Ultimate) (a, b)
Metallic pressure vessels	1.50	1.25	1.40	1.40
	Between 1.50 and 2.00	$\frac{1 + \text{Burst Factor}}{2}$		
	Greater than 2.00	1.50		

Table 3.4 Factor of safety requirement for pressure vessels as specified by ansi/aiaa s-080a-2018 [6].

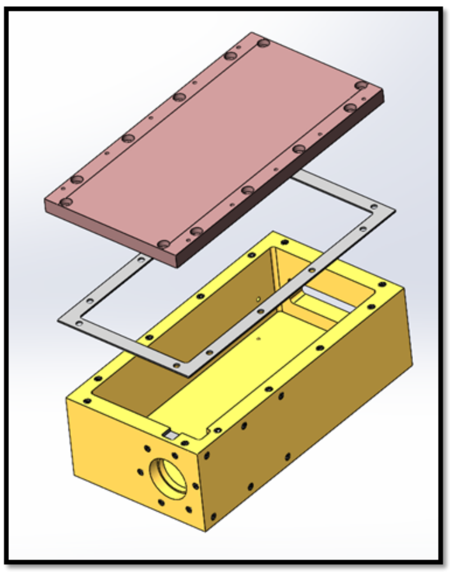

(a) IRCSP Housing gasket

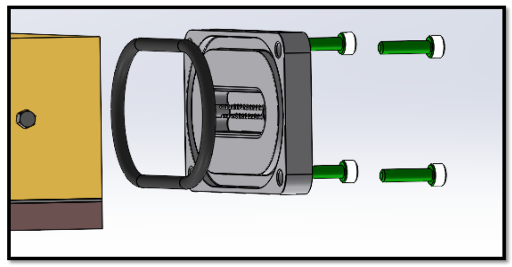

(b) Rear Connector seal

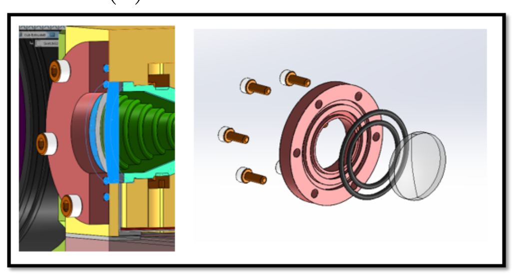

(c) Front lens seal

Figure 3.13 The IRCSP is hermetically sealed to prevent humidity ingress. In (a) a single gasket seals the main enclosure lid. In (b) a single O-ring seals the rear electrical connector. In (c) two O-rings seal the front lens.

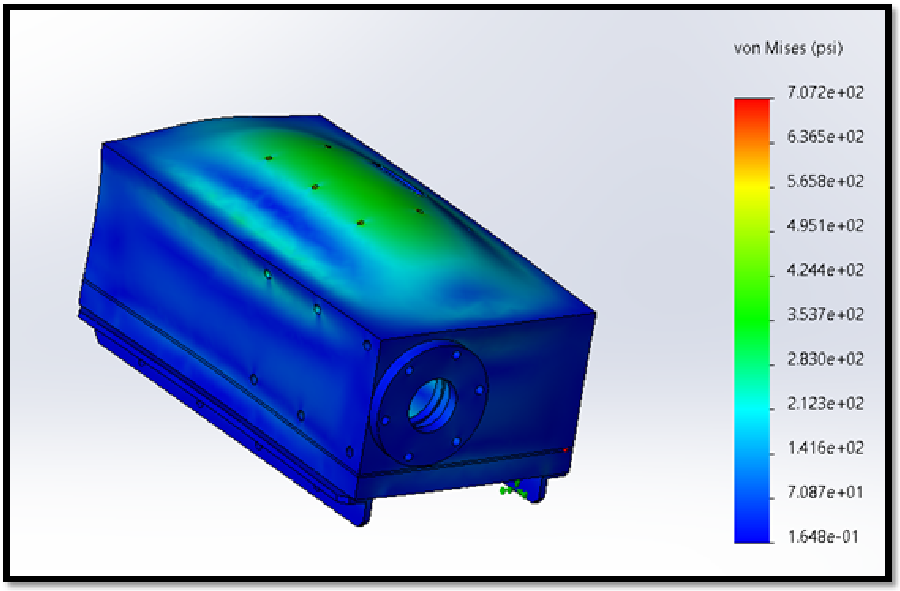

Figure 3.14 FEA modeling of the IRCSP pressure vessel to ensure the mechanical stress does not exceed the yield strength of the housing material. The maximum observed stress was 707.2[psi].

A pressure proof test was performed post-fabrication to ensure the efficacy of the rubber seals. The IRCSP was pressurized to 30 psi, over twice the expected maximum pressure during flight, and left over a three-day period. The enclosure held this pressure for the full duration of the test without any changes in the pressure being below the resolution of the pressure gauge.

3.5 Environmental Management

Thermal management at high altitude poses significant challenges. In low-pressure environments there is little to no participating media for convective or conductive cooling to occur, leaving only radiation [30, 31, 32, 33, 34]. U.S. Standard Atmo-

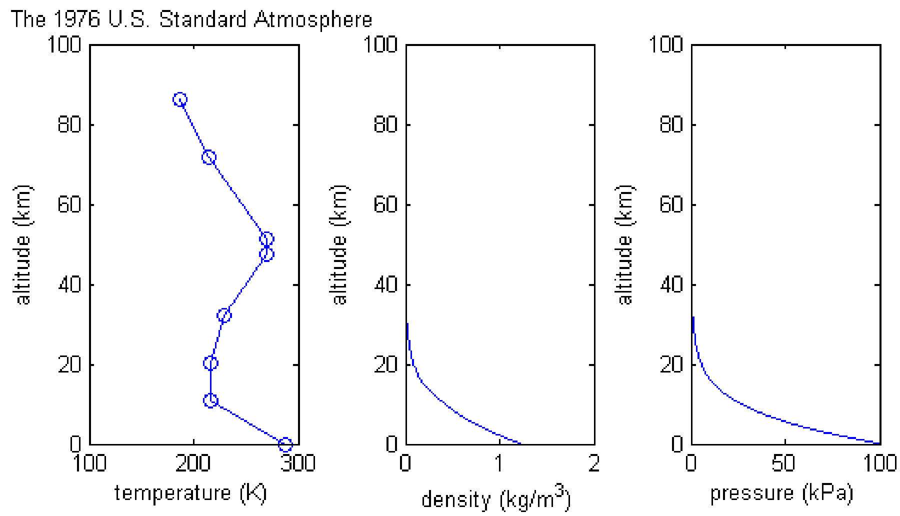

Figure 3.15 Temperature, pressure, and density as a function of altitude per the 1976 US Standard Atmosphere model. Reproduced from Wikipedia [3].

sphere model was used to model the static properties of the atmosphere as a function of altitude, h, in meters. The temperature T(h), pressure p(h), and density ρ(p,T) are modeled as a set of piece-wise linear functions. The ascent rate of the balloon provided by CSBF is 1000 ft/min.

$$T_{amb}(\mathrm{h})[^{\circ}C] = \begin{cases} 15.04 - 0.00649\mathrm{h} & 0 \leq \mathrm{h} < 11000 \\ -56.46 & 11000 \leq \mathrm{h} \leq 25000 \\ -131.21 + 0.02299\mathrm{h} & 25000 < \mathrm{h} \end{cases} \tag{3.1}$$

$$p(T_{amb})[KPa] = \begin{cases} 101.29 \left[\frac{T_{amb}+273.1}{288.08}\right]^{5.256} & 0 \leq \mathrm{h} < 11000 \\ 22.65e^{1.73-0.000157\mathrm{h}} & 11000 \leq \mathrm{h} \leq 25000 \\ 2.488 \left[\frac{T_{amb}+273.1}{216.6}\right]^{-11.388} & 25000 < \mathrm{h} \end{cases} \tag{3.2}$$

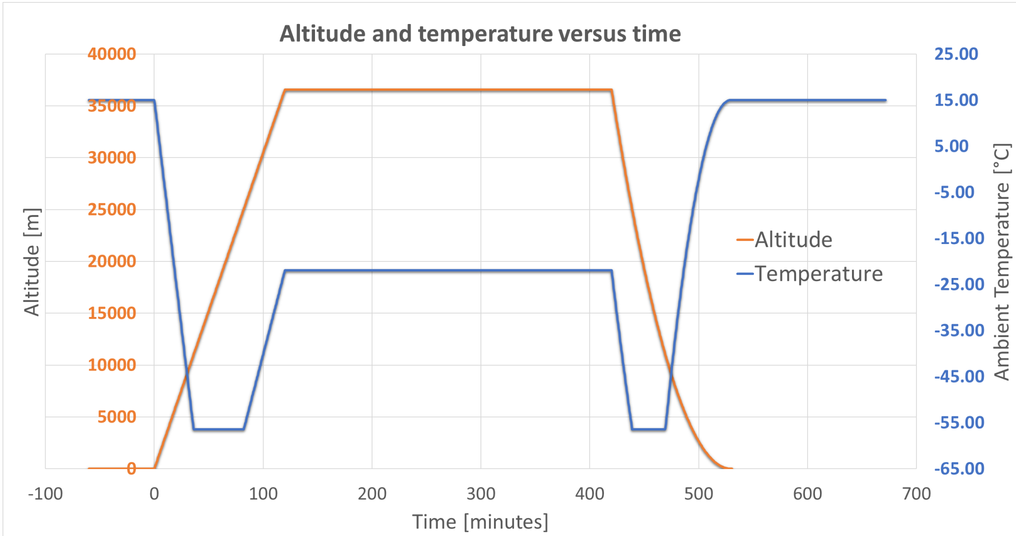

Figure 3.16 Altitude and ambient temperature as a function of time. Modeled with the US Standard Atmosphere and reported ascent rate of 1000 [ft/min].

$$\rho = \frac{p}{0.2869(T_{amb} + 273.1)} \tag{3.3}$$

Atmospheric pressure is expected to be as low as 0.04 [psi] during the balloon's time at float altitude leaving some plausible amount of non-radiative cooling. The atmosphere model presents a formula for the thermal conduction equation as a function of altitude. The conduction coefficient is evaluated at the film temperature, $T_F = 0.5(T_{HS} + T_{AMB})$

$$k = \frac{T_F^{3/2} 2.64638 \times 10^{-3}}{T_F + 245.4 \times 10^{-12/T_F}}. \tag{3.4}$$

The coefficient of thermal convection is estimated through various dimensionless numbers common to thermal and fluid dynamics. For free convection on a vertical wall, the coefficient is given as directly proportional to the Nusselt number, Nu, which is a function of the Rayleigh, Ra, and Knudsen, Kn, numbers [27, 31, 30, 32]. During ascent, the relative wind speed may be prominent enough to warrant modeling force convection. However, ascent is of little importance for the science goal of cloud top imaging and the neglect of forced convection offers a more pessimistic model.

$$h_{convection} = \frac{kNu}{L} \tag{3.5}$$

Where L is the characteristic length, taken as the vertical height of the radiator fins, $L = 0.0254[m] = 1[in]$.

$$Nu = 0.092 Ra^{0.134} Kn^{-0.263} \tag{3.6}$$

The Rayleigh number is dependant on various atmospheric properties and the characteristic length

$$Ra = \frac{\rho\beta}{\nu\alpha}(T_{HS} - T_F)L^3. \tag{3.7}$$

where β is the coefficient of thermal expansion approximated as $1/T$ for an ideal gas. Acceleration due to gravity, g, is held constant at $9.81 m/s^2$. The thermal diffusivity, α, is calculated form the specific heat of air, $c_{p_{air}}$, and density, ρ.

$$\alpha = \frac{k}{\rho c_{p_{air}}} \tag{3.8}$$

The kinematic viscosity, ν, is given as the ratio of dynamic viscosity, μ, to density, $\nu = \mu/\rho$.

$$\mu = B\frac{T_F^{3/2}}{T_F + S}. \tag{3.9}$$

Where B is a constant valued at 1.458×10^{-6} and S is the Sutherland constant of 110.4 [K][27]. The Knudsen number is a dimensionless parameter dependant on the mean-free path of the molecules in the fluid, D

$$Kn = \frac{D}{L}. \tag{3.10}$$

The mean free path is calculated from the atmospheric pressure, Boltzmann Constant, $K_B = 1.380649 \times 10^{-23}[J/K]$, Film temperature and average collisions diameter of the fluid particles, $d = 3.65 \times 10^{-10}[m]$ [27, 32, 30]

$$D = \frac{K_B T_f}{\sqrt{2}\pi d^2 P}. \tag{3.11}$$

The enclosure incorporates an increased thermal mass and thermo-electric cooler (TEC) to prevent thermal shock and aid in thermal regulation. Other systems such as sterling coolers, passive radiators, and nitrogen dewars were investigated. Sterling systems have low energy transfer rates that are on the order of the IRCSP power output, however these systems proved early on to be extremely cost-prohibitive [35]. Nitrogen Dewar systems are far too costly and complex to be feasible for this project [36, 37]. Exploration into passive thermal management with balancing radiative and convective cooling surface area with fine-tuned insulation could not provide the required temperature stability without complex retractable radiator systems [38].

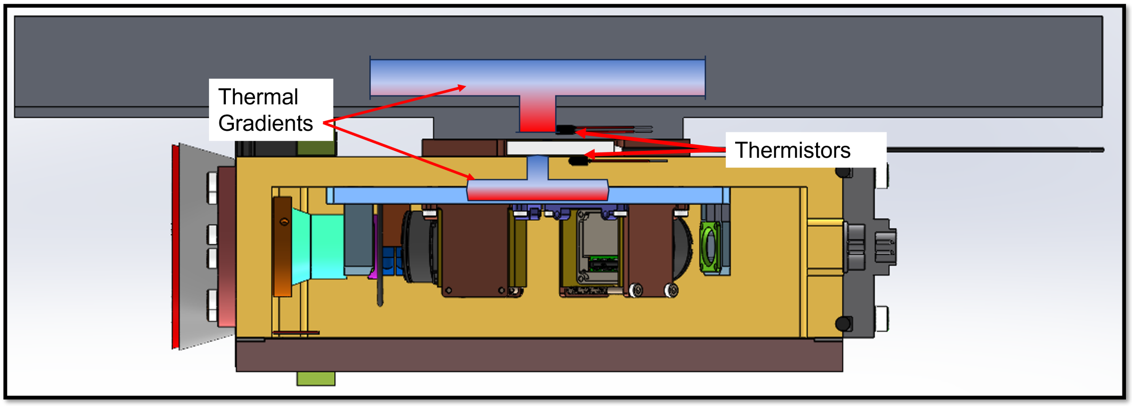

Figure 3.17 Cut-away of IRCSP enclosure showing expected thermal gradients for temperature regulation. 1″ of rigid polystyrene foam insulation with an R value of 5 surrounds the enclosure. Two thermistors are placed in close proximity to the TEC to monitor the temperature difference.

The TEC with a COTS PID controller was thus settled on for their appropriate cooling capacity, low SWaP, and ease of integration. The TEC pumps heat from the enclosure to a finned heatsink with large radiative area to maximize emission while also taking advantage of small amounts of convective and conductive cooling at high-altitude.

The instrument was modeled as a rectangular block of aluminum with dimensions roughly matching the enclosure and mass of $m_{enc} = 2.2[kg]$ as reported by the SolidWorks simulation model. The instrument is treated as completely encased in 1″ of polystyrene foam insulation with an R-Value of $0.88 \left[{}^{\circ}C\frac{m^2}{W}\right] \equiv 5 \left[{}^{\circ}F\frac{ft^2}{Btu}\right]$ which is in perfect thermal contact with the enclosure. The heat transported through the insulation is assumed to be fully dissipated upon reaching the external surface. The specific heat of aluminum is given as $C_{p_{AL}} = 0.9[J/{}^{\circ}Cg]$.

The total power entering the radiator is the power used to drive the TEC plus the

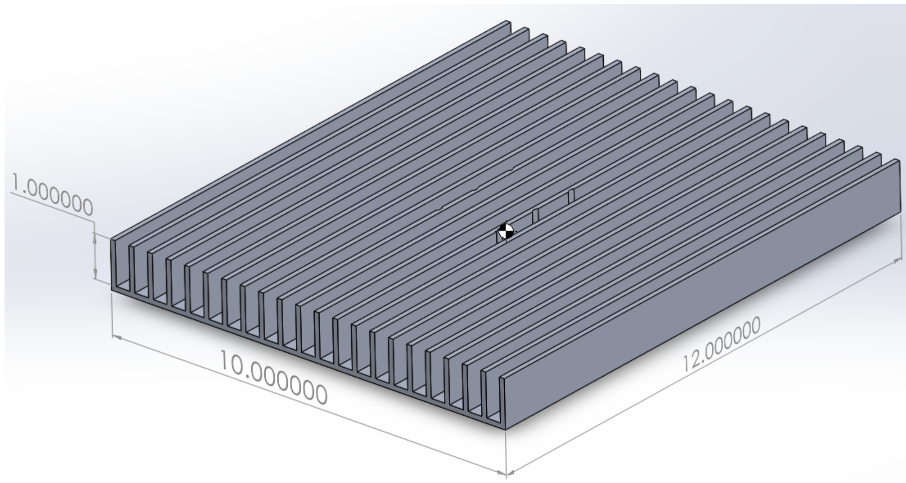

Figure 3.18 The large area radiator has a $10'' \times 12''$ footprint with $1''$ tall fins. There are 22 fins, each being $0.118''$ thick.

heat pumped by the TEC and the absorbed solar irradiance over the projected area of the radiator as seen by the sun, $A_\alpha[m^2]$. The heat dissipated by the radiator is done through thermal radiation from the outward-facing surface area, $A_\epsilon[m^2]$, with convective and conductive cooling from the total surface in contact with the air, $A_c[m^2]$ [30, 32]. Radiator dimensions are presented in Figure 3.18 with calculated values for the heat transfer areas presented in Table 3.5.

Cooling Area	Surfaces used	Value
Convective Area A_c	Total footprint and all 44 fin surfaces	0.248 $[m^2]$
Conduction Area A_c	Total footprint and all 44 fin surfaces	0.248 $[m^2]$
Emission Area A_ϵ	Total footprint and two fin surface	0.096 $[m^2]$
Absorption Area, A_α	Total footprint and one fin surface	0.080 $[m^2]$

Table 3.5 The areas used in modeling heat transfer into and out of the radiator. Convective and conductive areas are treated as the total area in contact with the fluid. Solar irradiance is absorbed over the full footprint with one fin illuminated while the emitting area includes both outward-facing fin surfaces.

$$q_{in} = V_{TEC}I_{TEC} + P_{TEC} + I(1-\rho)\alpha A_{\alpha} \tag{3.12}$$

$$q_{out} = -h_c A_c (T_{HS} - T_F) - \epsilon A_{\epsilon} \sigma \left({T_{HS}}^4 - {T_{amb}}^4 \right) \tag{3.13}$$

Where I is the solar irradiance at the top of the atmosphere, α and ϵ are the absorptivity and emissivity of the heat sink, respectively. The total heat transfer coefficient is h_c. T_{HS} and T_{AMB} are the temperature of the heat sink and ambient environment and σ is the Stefan-Boltzmann constant. V_{TEC} and I_{TEC} are the voltage and current required to drive the TEC. One critical simplification of this model is that the power consumed in driving the TEC is fixed at 24 Watts, $I_{TEC} = 2[A]$. The driving power will dependent on the difference between target and set temperature of the enclosure per the design of the PID loop. Therefore, the power entering the radiator will be dynamic and likely lower on average than .... The radiator temperature is modeled as

$$T_{HS_{n+1}} = T_{HS_n} + \frac{t_{n+1} - t_n}{C_{p_{AL}} m_{HS}} \left(q_{in} + q_{out} \right). \tag{3.14}$$

Each science camera is rated to output as low as 0.5 Watts. These cameras are powered over USB 2.0. The maximum voltage and current of a typical USB 2.0 port, 5V at 0.5A, was used to get an upper estimate of the cooling power required, $P_{cam} = 5[W]$. Based on the supplier data sheet, the heat pumped by the TEC is modeled as a linear function of the temperature difference between the cold side (enclosure) and hot side (radiator) of TEC. This model does not consider the spatial distribution of temperature. The radiator is treated as uniform temperature and thus the "hot side" temperature is lower than it would be during flight. When the TEC is coupled to the localized temperature of its contact area with the radiator, the most optimistic performance will be obtained.

$$P_{TEC} = \begin{cases} 20 & 0 > \Delta T \\ -\frac{1}{3}(T_{HS} - T_{enc}) + 20 & 0 \leq \Delta T \leq 60 \\ 0 & 60 < \Delta T \end{cases} \tag{3.15}$$

The enclosure temperature will change according to the dissipated camera power, the cooling power of the TEC, and the flux through the insulation. The flux through the insulation, Q, is given a function temperature difference between the enclosure and ambient and the R-value of the insulation

$$Q = \frac{(T_{amb} - T_{enc})}{R} \left[\frac{W}{m^2}\right]. \tag{3.16}$$

Spatial distribution of temperature was ignored and the heat transfer was limited to temporal dynamics

$$\frac{d}{dt}T_{enc} = \frac{(P_{cam} - P_{TEC} + QA)}{C_{p_{AL}} m_{enc}}. \tag{3.17}$$

This differential equation was treated as a discrete, recursive formula and plotted with a temporal resolution of $t_{n+1} - t_n = 30[s]$.

$$T_{enc_{n+1}} = T_{enc_n} + \frac{t_{n+1} - t_n}{C_{p_{AL}} m} \left(P_{cam} - P_{TEC} + \frac{(T_{amb} - T_{enc_n})}{R} A\right) \tag{3.18}$$

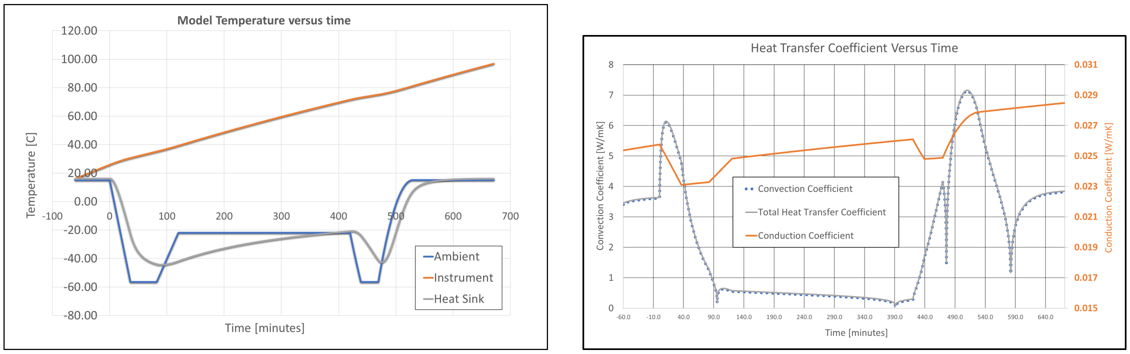

(a) Thermal behavior with no cooling (b) Heat transfer coefficients with no cooling

Figure 3.19 In (a) radiator and IRCSP thermal behavior over the course of the expected flight with no cooling system. This model includes insulation on the IRCSP and solar irradiance on the radiator. In (b) convective and conductive cooling coefficients over the course of the expected flight.

Various conditions were modeled to determine the best set temperature and switching conditions for the flight. There is potential for condensation to form on the exterior lens at low altitudes then freeze during ascent and thus blocking our desired signal. To mitigate this, altitude was explored to be a switching constraint in which the TEC would change from a high temperature to a low temperature above 15 [km]. This would allow the instrument to remain well above the dew point until the absolute humidity decreased enough to no longer be a concern. Based on this simulation, the operating temperature for the full duration of the flight is set to $+20°C$.

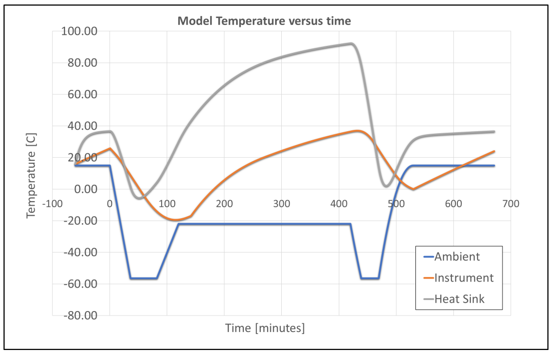

(a) C Cap

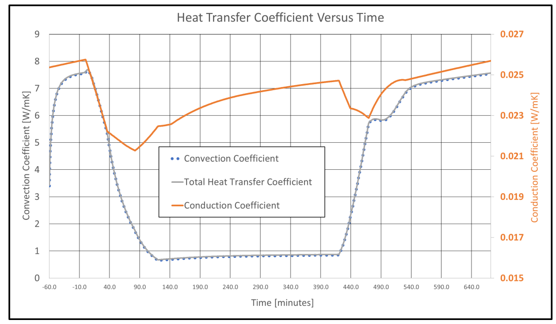

(b) D Cap

Figure 3.20 In (a) IRCSP thermal behavior over the course of the flight with no constraints on the cooling system. The TEC is continuously powered with 24 Watts from t = -60 minutes with no minimum or maximum temperature boundaries.

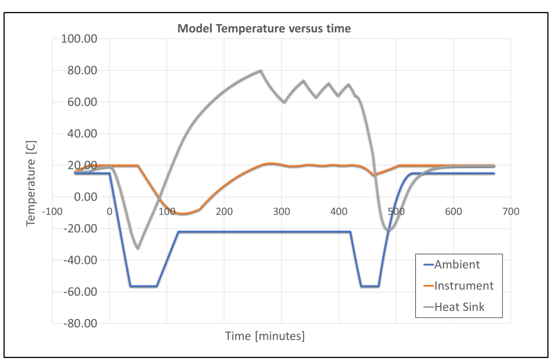

(a) C Cap

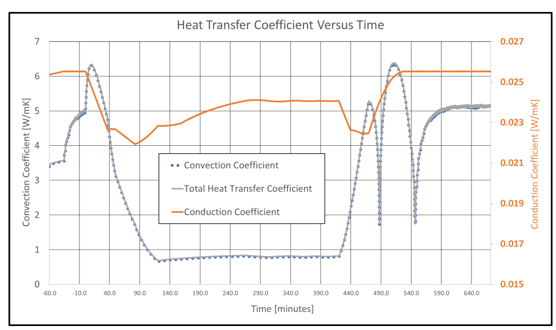

(b) D Cap

Figure 3.21 Thermal behavior with the IRCSP set to only cool above 15 [km] with a ground temperature of 20 °C. In (b), resulting heat transfer coefficients.

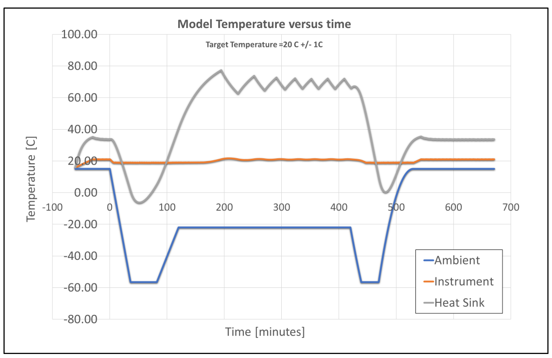

(a) Thermal behavior with no cooling

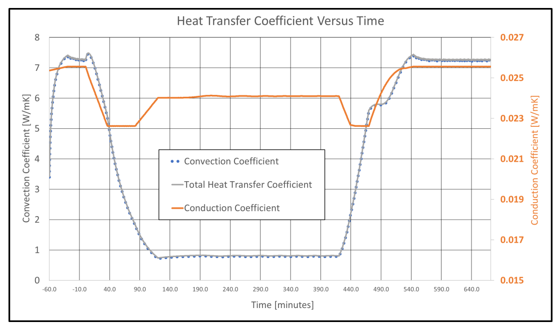

(b) Heat transfer coefficients with no cooling

Figure 3.22 In (a) The IRCSP thermal behavior with a minimum allowable temperature of $19°C$ and maximum temperature of $21°C$. In (b) convective and conductive cooling coefficients over the course of the expected flight under these temperature constraints.

CHAPTER 4

Mueller Polarimetry for Quantifying the Stress Optic Coefficient in the Infrared

The Stress Optic coefficient can be quantified by a series of retardance measurements given a known loading force. Plotting the measured birefringence as a function of applied stress provides the stress optic coefficient as the slope. Combining Equations 2.3 and 2.16 shows the relation between measured retardance and calculated stress

$$\frac{\delta^\circ}{360^\circ}\frac{\lambda}{t} = C(\sigma_1 - \sigma_2). \tag{4.1}$$

In this work, the wavelength λ is set to $1550 \pm 0.1[nm]$, t is the sample thickness, measured with calipers to be $2.17 \pm 0.025[mm]$. The principal stresses are extracted from FEA models and a linear fit is used to interpolate stress values at intermediate applied forces. To apply a stress during the measurement, a simple fixture is created to support weight and load the sample in compression with an increasing force; see Figure 4.4. The sample is compressed between a weight-supporting platform and a precision load cell, which reads the applied force. Some samples were measured at forces as low as 5 [N]; however, large uncertainties and non-linear effects were observed. For this reason, low-magnitude forces are abandoned, leaving five values: 191, 244, 280, 326, and 357 [N].

4.1 Stress Application and Modeling

Stress fields resulting from an applied force are a well-characterized phenomenon [17, 39, 40, 26, 41]. The loading case relevant to this work is a cylindrical part loaded with diametrically apposed concentrated force and a plane stress approximation. This approximation is valid as the z-axis stress is decoupled from x and y for light propagating along the z-axis, allowing the assumption of zero stress in the z-direction[25]. The stress fields were simulated with both an analytical model and FEA in Solidworks. In Cartesian coordinates, the stress fields for a diametrically loaded cylinder of radius, r, and loading force, f, are modeled using Equations 4.2, 4.3 and 4.4 [17, 24, 39, 41].

$$\sigma_{xx} = -\frac{2f}{\pi t}\left(\frac{(r-y)x^2}{\left((r-y)^2+x^2\right)^2} + \frac{(r+y)x^2}{\left((r+y)^2+x^2\right)^2} - \frac{1}{2r}\right) \tag{4.2}$$

$$\sigma_{yy} = -\frac{2f}{\pi t}\left(\frac{(r-y)^3}{\left((r-y)^2+x^2\right)^2} + \frac{(r+y)^3}{\left((r+y)^2+x^2\right)^2} - \frac{1}{2r}\right) \tag{4.3}$$

$$\tau_{xy} = \frac{2f}{\pi t}\left(\frac{(r-y)^2x}{\left((r-y)^2+x^2\right)^2} - \frac{(r+y)^2x}{\left((r+y)^2+x^2\right)^2}\right) \tag{4.4}$$

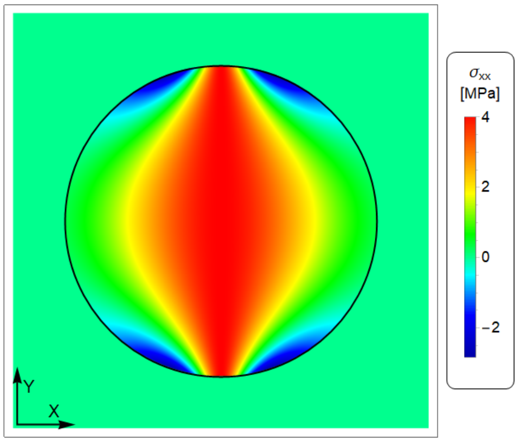

(a) Stress distribution for σ_{xx}

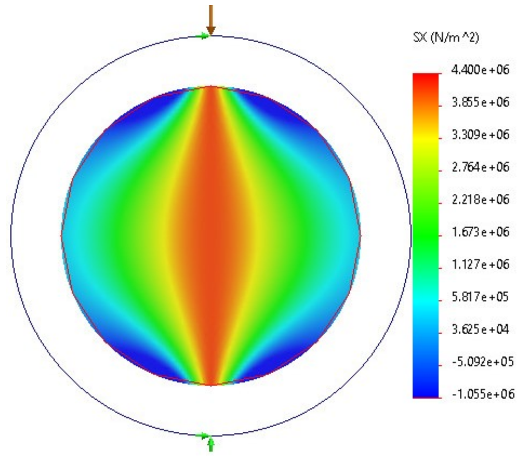

(b) Stress field for σ_{xx}

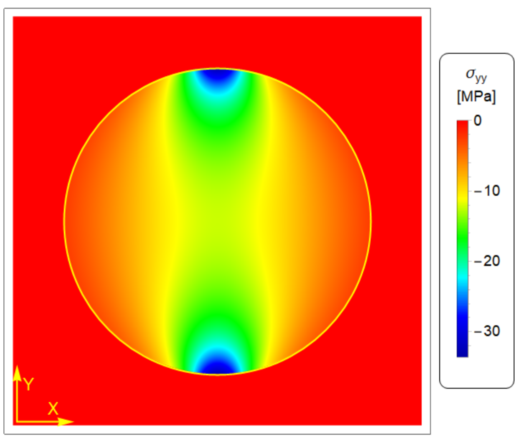

(c) Stress distribution for σ_{yy}

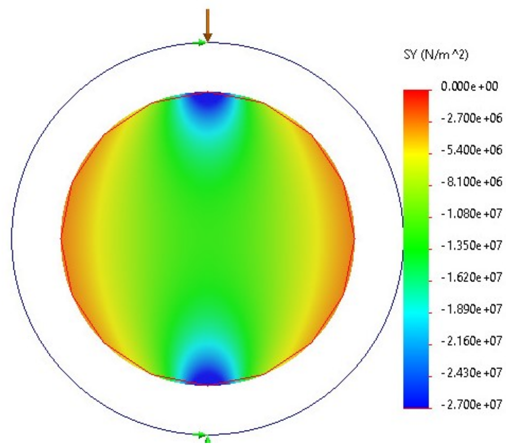

(d) Stress distribution for σ_{yy}

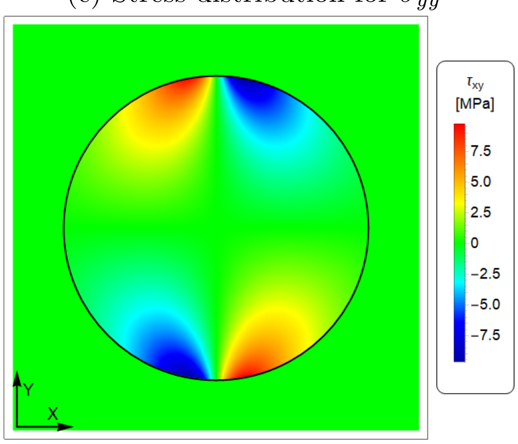

(e) Stress distribution for τ_{xy}

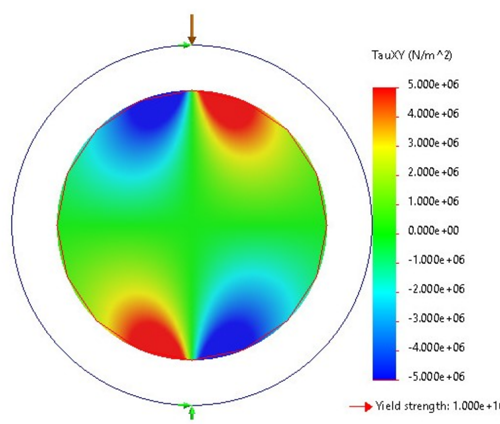

(f) Stress distribution for τ_{xy}

Figure 4.1 Comparison of stress fields for the closed form solution (left column) and the FEA model (right column) under 357 [N] loading condition. The sections are clipped to 75% of the physical diameter to mask extreme values.

The polarization orientation is defined such that horizontal polarization is along the x-axis. The expectation is that the refractive index in the y-direction will be increased with the index in the x-direction being decreased and that of the z-direction having no effect on the incident signal [25, 14, 20, 42]. Figure 4.1 shows the stress fields for normal and shear components from both the closed-form analytical model and the FEA simulation. To estimate the retardance resulting from the applied stress, the reported value for the stress optic coefficient of N-BK7 is used with the analytical model for the principal stresses. Figure 4.2 shows the stress fields for principal stresses from both the closed-form analytical model and the FEA simulation.

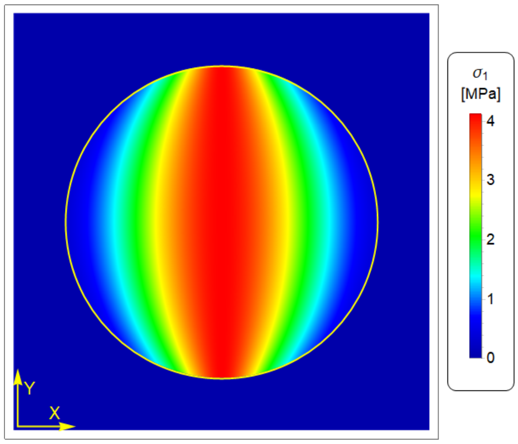

(a) CalculatedStress distribution for σ_1

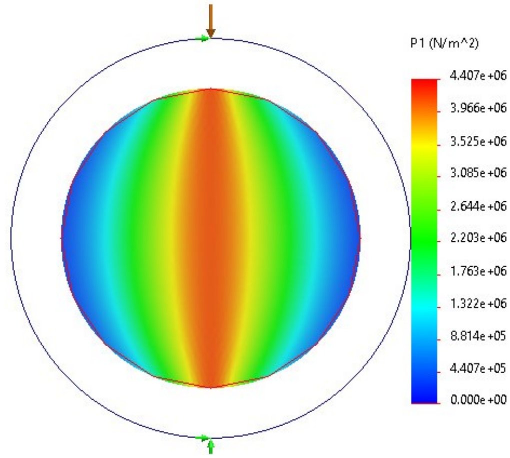

(b) FEA Stress field for σ_1

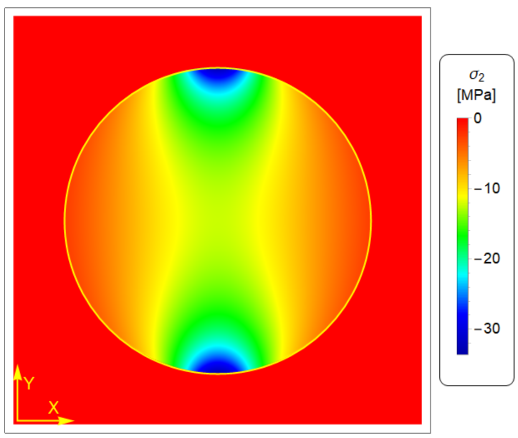

(c) CalculatedStress distribution for σ_2

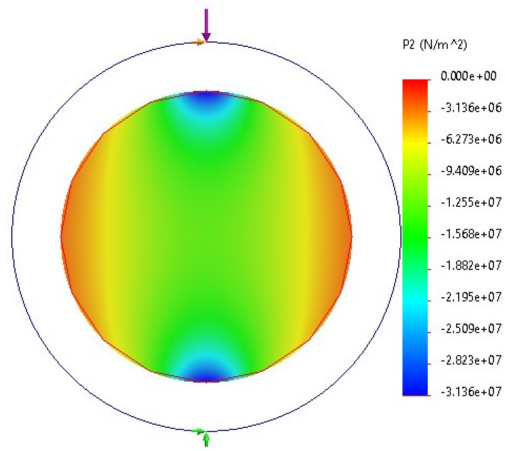

(d) FEA Stress field for σ_2

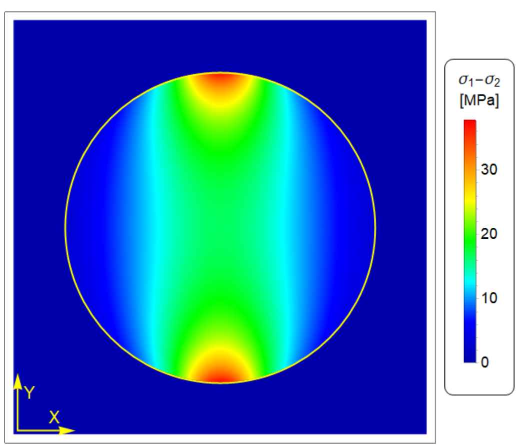

(e) Calculated Stress field for $\sigma_1 - \sigma_2$

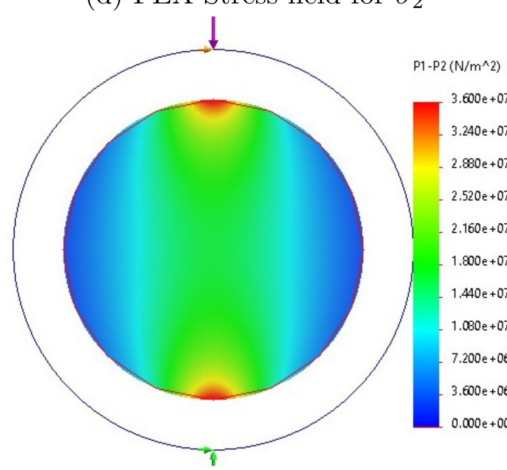

(f) FEA Stress distribution for $\sigma_1 - \sigma_2$

Figure 4.2 Comparison of principal stress fields and principal stress difference for the closed form solution (left column) and the FEA model (right column) under 357 [N] loading condition. The sections are clipped to 75% of the physical diameter to mask extreme values.

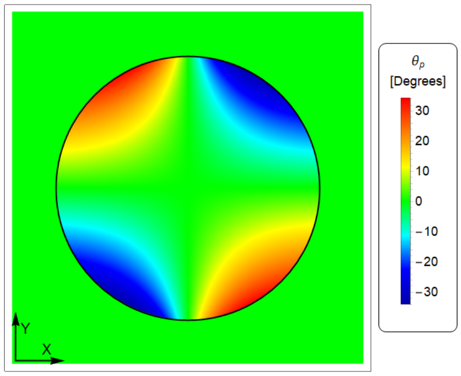

(a) Calculated Fast axis orientation

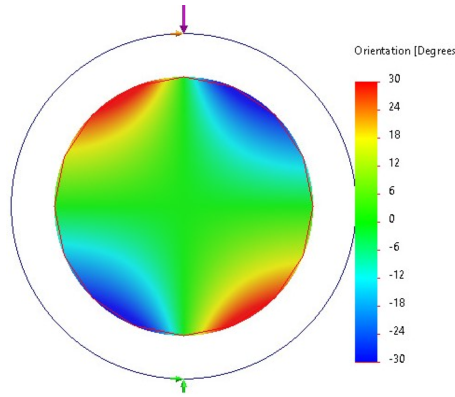

(b) FEA Fast axis orientation

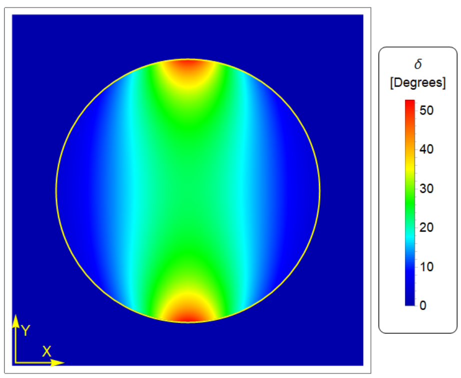

(c) Calculated Retardance, $\delta°$

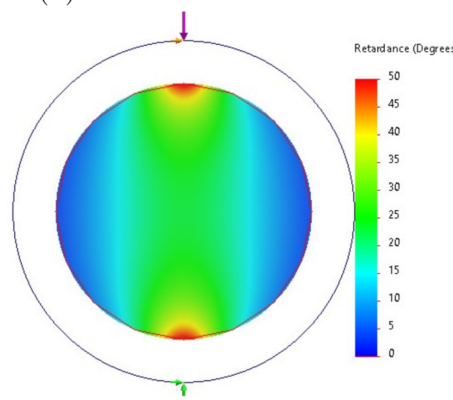

(d) FEA Retardance, $\delta°$

Figure 4.3 Retardance magnitude and fast axis orientation for N-BK7 under 357 [N] of force. The reported stress optic coefficient of $2.77[TPA]^{-1}$ was used in this modeling.

4.2 Near Infrared Mueller Matrix Imaging System

Mueller polarimetry as a tool for measuring a stress optic coefficient offers improved polarimetric accuracy, fewer assumptions about the sample's optical properties, and information useful for identifying experimental deviations from the intended applied force. Stress optic coefficient measurements do not require Mueller polarimetry. Assuming the sample is a pure linear retarder and rotating polarization components to the orientations of minimum and maximum transmission is the simplest possible experiment to quantify the stress optic coefficient [43, 25]. Mueller polarimetry quantifies all polarimetric properties of a sample: retardance, diattenuation, and depolarization. The linear retardance estimate from Mueller polarimetry is computed from a series of over-determined polarimetric measurements. The polarimetric accuracy can be improved by increasing the number of measurements in this series [44].

Imaging the spatial distribution of the Mueller matrix across the sample offers further advantages toward quantifying the stress optic coefficient and assessing experimental conditions. The stress field is expected to be in-homogeneous across the sample. Imaging the pattern of birefringence allows comparison between the assumed and observed stress patterns. The line of action can be identified from a Mueller image. A region of the sample where the expectation of a fast-axis perpendicular to the line of action can be identified. Imaging can also identify defects and regions of residual stress within the sample.

The Near InfraRed POLarimeter (NIRPOL) consists primarily of a collimated source, reference detector, polarization state generator (PSG), polarization state analyzer (PSA), and camera; see figure 4.4. The PSA and PSG each contain a static COTS linear polarizer and a rotating custom true zero-order $\lambda/3$ waveplate. To remove source power fluctuation effects, a reference detector is used prior to the PSG. A He:Ne laser is used to ensure all optical elements and each SUT are placed

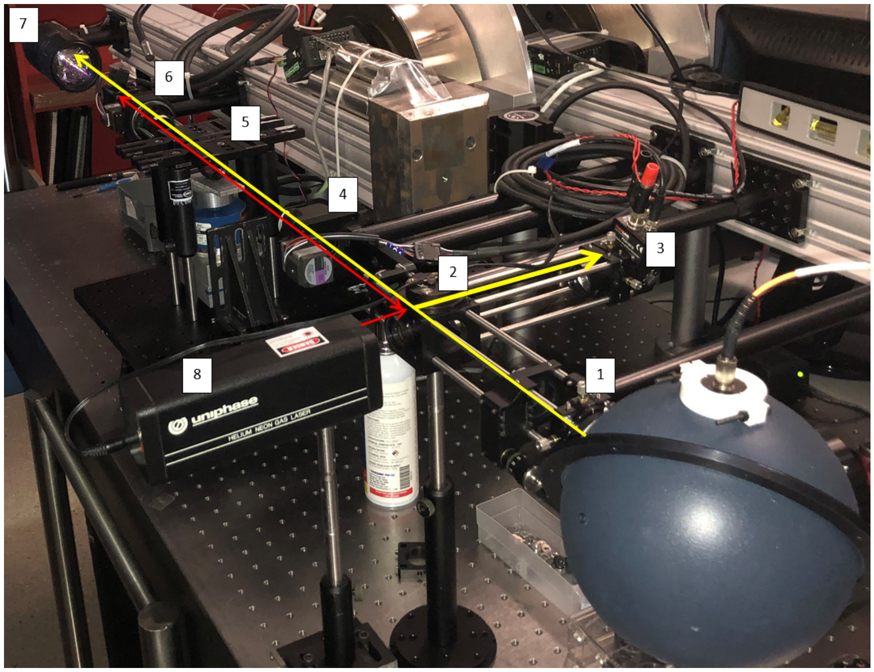

(a) NIRPOL Polarimeter with critical parts labeled.

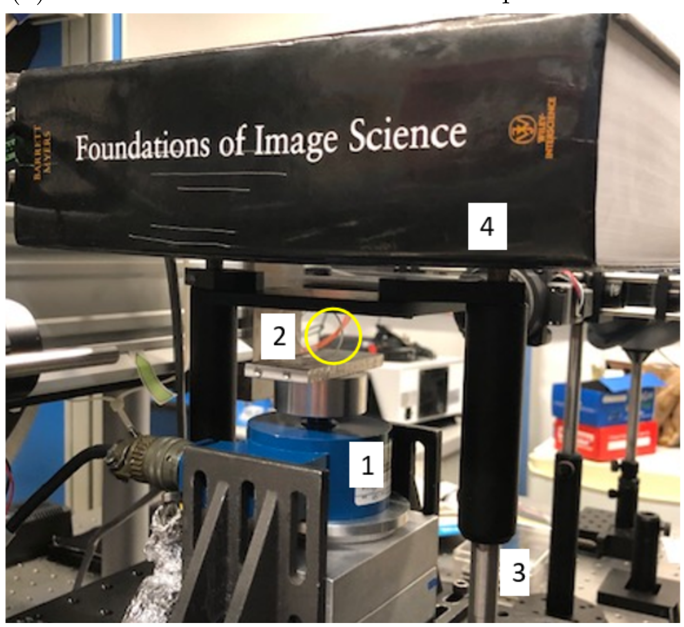

(b) Fixture for Diametric Loading the sample during measurement.

Figure 4.4 NIRPOL instrument layout in (a) (1) integrating sphere with adjustable aperture and collimating lens; (2) beamsplitter for reference detection and He:Ne alignment laser; (3) reference detector; (4) PSG; (5) sample space with force application fixture; (6) PSA; (7) InGaAs camera and imaging lens; (8) He:Ne alignment laser. In (b) (1) precision load cell for reading force; (2) sample under test within yellow circle; (3) Optical posts as guide rails to prevent tilting or twisting; (4) platform for supporting stress-inducing load.

at normal incidence to the source beam. The camera is an InGaAs detector with an adjustable focal length lens. The camera is mounted at a 90° angle effectively rotating the measurement frame. For all subsequent measurements, the y-axis is running horizontal in the image. Stress-induced birefringence is usually spatially-dependent across a sample [14]. For this reason, the imaging capabilities of NIRPOL are important to select a region of uniform linear retardance magnitude and the expected retardance orientation relative to the line of action, see figure 4.6. Furthermore, any residual stress or manufacturing defects in the material would become obvious in the measured retardance distribution.

4.3 Polarimetric Data Processing

NIRPOL measures a sequence of 64 images at varying PSG and PSA configurations. The fast-axis orientations for the PSG and PSA retarders rotate over the measurement sequence [45]. These 64 measurements create a system of linear equations which relate the images to the 16 Mueller matrix elements. The pseudo-inverse of this over-determined linear system reconstructs the Mueller matrix. For the n^{th} measurement in the sequence of 64 measurements, the Mueller matrices of the PSG and PSA are

$$\mathbf{G}_n = \mathbf{LR}(n \times 5.625^\circ + \theta_g, \delta_g)\mathbf{LP}(0^\circ) \tag{4.5}$$

Item	Manufacturer	Model	Serial Number
Source	Photonetics	Tunics-Plus 3642 HE 10	10 5686
Camera	Allied Vision	Goldeye G-008 SWIR TEC	00219
Reference Detector	Thor Labs	InGaAs amplified detector PDA10CS	N/A
Imaging Lens	Edmund Optics	SWIR Fixed Focal Length Lens 83-170	N/A
Force Gauge	Interface	1600 Gold Standard 16068GR-209	483858
PSA/PSG Linear Polarizer	Moxtek	Wire-Grid IR Polarizer BIR05A	N/A
PSA/PSG Retarders	Casix	Custom $\lambda/3$ achromatic waveplate	N/A
Waveplate rotating motors	Oriental Motor	Hollow Rotary Actuator DGM60-ARAK	N/A

Table 4.1 Parts list for the NIRPOL instrument.

and

$$\mathbf{A}_n = \mathbf{LP}(\theta^\circ_{LP})\mathbf{LR}(n \times 5.625^\circ \times 4.91 + \theta_a, \delta_a) \tag{4.6}$$

where $\mathbf{LP}$ is the Mueller matrix of an ideal linear polarizer and $\mathbf{LR}(\theta, \delta)$ is a linear retarder with θ fast-axis and δ magnitude. The orientation of the PSG linear polarizer is 0° by definition and defines the frame of reference. All subsequent axis orientations are defined relative to this axis. The orientation of the PSA linear polarizer is θ_{LP}. The fast-axis orientations for the PSA and PSG retarders prior to rotation (*i.e.* $n = 0$) are denoted θ_a and θ_g; respectively. The PSA and PSG retardance magnitudes are given by δ_a and δ_g; respectively. The PSG retarder rotates 5.625° between n and $n+1$ of the measurement sequence. The PSA retarder rotates 4.91 times the rate of the PSG retarder, or 27.62° between consecutive measurements. The optimization of the condition number of the pseudo-inverse matrix determines these rotation rates. Consider inserting a sample with Mueller Matrix $\mathbf{M}$ between the PSG and the PSA. The Mueller matrix of the entire system at the n^{th} measurement in the sequence is given by

$$\mathbf{M}_n = \mathbf{A}_n\, \mathbf{M}\, \mathbf{G}_n \tag{4.7}$$

The Mueller matrix of the system transforms the polarization state of the source into the polarization state incident on the detector, as in

$$\mathbf{S}_n = \mathbf{M}_n \mathbf{S}_s \tag{4.8}$$

where $\mathbf{S}_s$ is the Stokes vector of the source and $\mathbf{S}_n$ is the Stokes vector of light incident on the detector. The detector measures the incident total flux, which is given by only the first element of the Stokes vector $\mathbf{S}_n = \begin{bmatrix} S_0 & S_1 & S_2 & S_3 \end{bmatrix}^\dagger$. Therefore, only the first row of $\mathbf{M}_n$ affects the n^{th} measurement, denoted p_n. The polarimetric measurement equation for this single measurement is

$$p_n = \mathbf{a}_n^\dagger \mathbf{M} \mathbf{g}_n = \mathbf{w}_n \mathbf{m} \tag{4.9}$$

where $\mathbf{a}_n$ is a row vector given by the top row of the Mueller matrix $\mathbf{A}_n$, also called the analyzer vector. Similarly, $\mathbf{g}_n$ is a column vector given by the first column of the Mueller matrix $\mathbf{G}_n$, also called the polarizance vector. The Mueller matrix of the sample $\mathbf{M}$ has been rearranged into a 16×1 column vector $\mathbf{m}$, and lower-case is used to denote this change from matrix to vector. Here $\mathbf{w}_n$ is a 1×16 row vector given by

$$\mathbf{w}_n = \mathbf{a}_n \otimes \mathbf{g}_n^{\dagger}. \tag{4.10}$$

The Kronecker product is denoted $\otimes$. If $\mathbf{C}$ is an $m \times n$ matrix and $\mathbf{B}$ is a $p \times q$ matrix, then the Kronecker product $\mathbf{C} \otimes \mathbf{B}$ is the $mp \times nq$ block matrix

$$\mathbf{C} \otimes \mathbf{B} = \begin{pmatrix} c_{11}\mathbf{B} & \ldots & c_{1n}\mathbf{B} \\ \ldots & \ddots & \ldots \\ c_{m1}\mathbf{B} & \ldots & c_{mn}\mathbf{B} \end{pmatrix}. \tag{4.11}$$

The series of 64 measurements are linearly related to the Mueller matrix of the sample by $\mathbf{p} = \mathbf{W}\mathbf{m}$. Here $\mathbf{p}$ is a 64×1 row vector of measurements and $\mathbf{W}$ is a 64×16 matrix, called the polarimetric measurement matrix, given by

$$\mathbf{W}(\theta_{LP}, \theta_a, \theta_g, \delta_a, \delta_g) = \begin{bmatrix} \mathbf{w}_0 \\ \mathbf{w}_1 \\ \vdots \\ \mathbf{w}_{64} \end{bmatrix} \tag{4.12}$$

where each row of this matrix is given by Equation 4.10. Here the dependence between $\mathbf{W}$ and the PSA/PSG parameters introduced in Equation 4.5 and 4.6 are denoted on the LHS. The five parameters of fit to a NIRPOL measurement of air.

From these five parameters derived from calibration, all rows of the polarimetric measurement matrix can be computed using Eqs. 4.9 and 4.10. The pseudo-inverse of the over-determined matrix **W** is used to reconstruct the Mueller matrix of the object from the measurement series. This calculation is performed pixel-wise to reconstruct the Mueller matrix image of the sample. The inverse of the polarimetric measurement matrix is often called the data reduction matrix. A popular figure of merit for optimizing retardance magnitude and rotation rates in rotating retarder polarimeters is the condition number [44]. The condition number equals the ratio of the largest to smallest singular values of a polarimeter's **W** matrix.

4.3.1 Alignment and Calibration

In the lab frame of reference, the PSG linear polarizer transmission axis is approximately horizontal or parallel to the optical bench depicted in figure 4.4. The precise orientation of the LP is not important as it is defined to be $0°$ as previously mentioned. The analyzer linear polarizer is aligned with its transmission axis parallel to the PSG LP but not strictly defined as $0°$ to allow for error correction in calibration. Both retarder fast axis at $n = 0$ are aligned to be parallel to PSG LP transmission axis but also left as a calibration fit parameter to allow for alignment correction. The waveplates are custom true zero-order $\lambda/3$ achromatic elements with a design wavelength of 1550 nm. The retardance magnitude of these elements is also a calibration fit parameter. The instrument is calibrated by measuring air. The Mueller matrix of air is expected to be an identity matrix, and thus deviations from unity are attributed to instrumental errors [44, 45, 14]. a least-squares fit is performed to calculate $\theta_{LP}, \theta_a, \theta_g, \delta_a$, and δ_g. A zero-load measurement is taken for each SUT to inspect for and calibrate out any residual stress from the manufacturing process.

4.3.2 Linear Retardance Analysis

Lu-Chipman decomposition is performed on the measured Muller matrix to isolate the pure retarder element. A general elliptical retarder is given by the Mueller matrix [14]

$$\mathbf{ER}(\delta_H, \delta_{45}, \delta_R) = \begin{bmatrix} 1 & 0 & 0 & 0 \\ 0 & \frac{\delta_H^2 + \left(\delta_{45}^2 + \delta_R^2\right)C}{\delta^2} & \frac{\delta_{45}\delta_H T}{\delta^2} + \frac{\delta_R S}{\delta} & \frac{\delta_H \delta_R T}{\delta^2} - \frac{\delta_{45} S}{\delta} \\ 0 & \frac{\delta_{45}\delta_H T}{\delta^2} - \frac{\delta_R S}{\delta} & \frac{\delta_{45}^2 + \left(\delta_R^2 + \delta_H^2\right)C}{\delta^2} & \frac{\delta_R \delta_{45} T}{\delta^2} + \frac{\delta_H S}{\delta} \\ 0 & \frac{\delta_H \delta_R T}{\delta^2} + \frac{\delta_{45} S}{\delta} & \frac{\delta_R \delta_{45} T}{\delta^2} - \frac{\delta_H S}{\delta} & \frac{\delta_R^2 + \left(\delta_{45}^2 + \delta_H^2\right)C}{\delta^2} \end{bmatrix}. \tag{4.13}$$

Here $C = \cos\delta$, $S = \sin\delta$, $T = 1 - \cos\delta$ and $\delta_H, \delta_{45}, \delta_R$ are the horizontal, 45°, and right circular retardance; respectively. While only linear retardance parameters are expected, for completeness, circular effects are included in this initial reduction. The total retardance magnitude δ without a subscript is

$$\delta = \sqrt{\delta_H^2 + \delta_{45}^2 + \delta_R^2} \quad S_{fast} = \frac{1}{\delta}\begin{bmatrix} 1 \\ \delta_H \\ \delta_{45} \\ \delta_R \end{bmatrix} \tag{4.14}$$

Where S_{fast} is an eigen polarization and the Stokes vector for the minimum index of refraction. The retarder components are calculated from the off-diagonal elements of the Mueller matrix in Equation 4.13.

$$(\delta_H, \delta_{45}, \delta_R) = \frac{\delta}{2\mathrm{sin}\delta}\left(M_{23} - M_{32}, M_{31} - M_{13}, M_{12} - M_{21}\right). \tag{4.15}$$

The linear retardance is calculated from only the horizontal and 45° retardance components.

$$\delta = \sqrt{\delta_H^2 + \delta_{45}^2} \tag{4.16}$$

The linear retardance magnitude is repeatedly computed from three separate trials for each force magnitude. To calculate the sample statistics on birefringence, the linear retardance mean and standard deviation are averaged over the three trials

$$\bar{\delta} \pm \varepsilon_{\bar{\delta}} = \frac{1}{3}\sum_{k=1}^{3}\delta_k \pm \sqrt{\frac{1}{3}\sum_{k=1}^{3}(\varepsilon_k)^2}. \tag{4.17}$$

Here δ_k and ε_k are the mean and standard deviation of linear retardance in a selected region for the k^{th} trial. To simplify the propagation of birefringence error, the retardance is converted from waves δ_w to length δ_λ

$$\delta_w \pm \varepsilon_{\delta_w} = \frac{\bar{\delta}}{360^\circ} \pm \frac{\varepsilon_{\bar{\delta}}}{360^\circ} \tag{4.18}$$

$$\delta_\lambda \pm \varepsilon_{\delta_\lambda} = \delta_w\lambda \pm \delta_\lambda\sqrt{\left(\frac{\varepsilon_{\delta_w}}{\delta_w}\right)^2 + \left(\frac{\varepsilon_\lambda}{\lambda}\right)^2} \tag{4.19}$$

where ε_λ is the uncertainty in wavelength; set to 0.1 [nm] in this work. Finally, the average birefringence and standard deviation is

$$\Delta n \pm \varepsilon_{\Delta n} = \frac{\delta_\lambda}{t} \pm \Delta n \sqrt{\left(\frac{\varepsilon_{\delta_\lambda}}{\delta_\lambda}\right)^2 + \left(\frac{\varepsilon_t}{t}\right)^2} \tag{4.20}$$

4.4 N-BK7 Example Measurement

		Run 1		Run 2		Run 3	
Force [N]	Stress [MPa]	δ°	ε_δ	δ°	ε_δ	δ°	ε_δ
191.90	8.620	10.424	0.237	10.893	0.165	10.662	0.391
244.75	10.996	13.805	0.223	13.869	0.204	13.243	0.407
280.65	12.608	16.417	0.175	16.070	0.173	15.425	0.417
326.15	14.652	19.432	0.170	18.841	0.159	19.168	0.198
357.75	16.071	21.336	0.193	20.863	0.264	21.349	0.223

Table 4.2 Raw data for measured linear retardance in degrees, for each applied Force.

Force [N]	Stress [MPa]	$\overline{\delta}^\circ$	$\varepsilon_{\overline{\delta}}$	$\Delta n (10^{-5})$	$\varepsilon_{\Delta n}(10^{-5})$
191.90	8.620	10.660	0.281	2.11	0.0557
244.75	10.996	13.639	0.293	2.71	0.0581
280.65	12.608	15.970	0.279	3.17	0.0555
326.15	14.652	19.150	0.176	3.80	0.0352
357.75	16.071	21.180	0.228	4.20	0.0455

Table 4.3 Average linear retardance $\overline{\delta}^\circ$, in degrees, and calculated birefringence (Δn) for each applied Force.

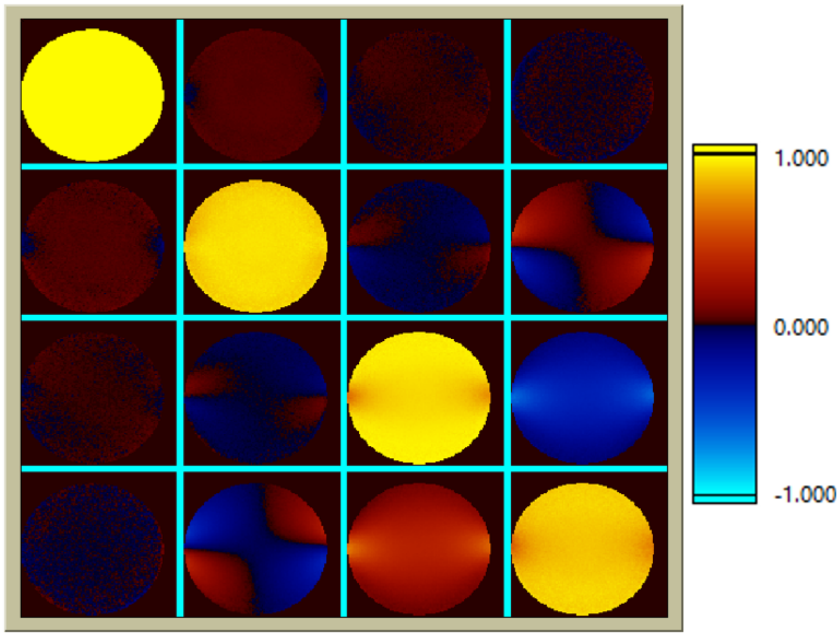

(a) Normalized Mueller Matrix

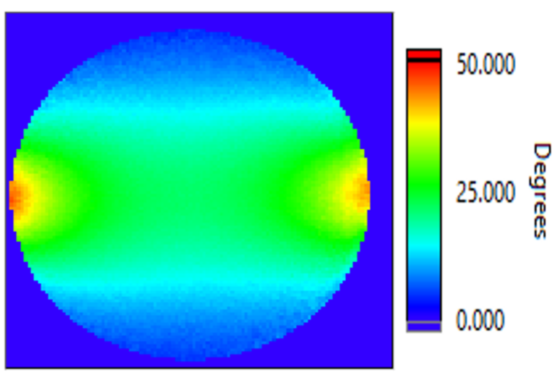

(b) Linear Retardance

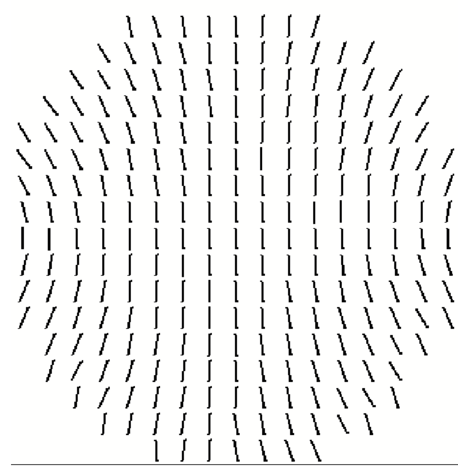

(c) Linear Retardance Orientation

Figure 4.5 NIRPOL measurements in (a) the normalized Mueller Matrix image of a 2.17 [mm] thick uncoated N-BK7 sample at 357.75 [N] of force. The line of action is approximately horizontal. In (b) the linear retardance of the sample is computed from the Mueller Matrix using methods detailed in Sec. 4.3.2.

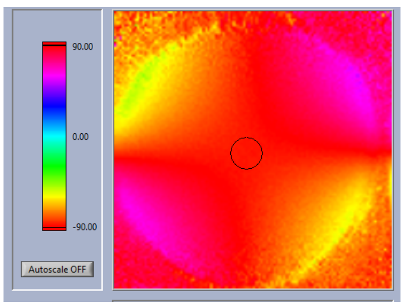

(a) 98 pixel ROI denoted by black circle

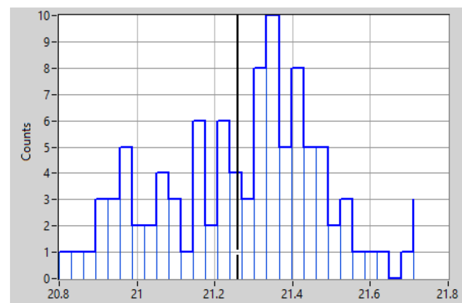

(b) Histogram of linear retardance in ROI

	Mean	Standard Deviation	Median
Linear Retardance	21.2390	0.2005	21.3048
Retardance Orientation	-87.6020	0.2892	-87.6346
Circular Retardance	-0.1033	0.2011	-0.0777
Horizontal Retardance	-21.1635	0.1981	-21.2260
45 Degree Retardance	-1.7759	0.2165	-1.7426
Retardance Magnitude	21.2402	0.2008	21.3051

(c) Statistics within ROI of Polarization Parameters

Figure 4.6 In (a) the NIRPOL graphic user interface (GUI) is used to display the retardance orientation and select a 98-pixel ROI where the fast-axis is perpendicular to the line of action. The cross pattern of the red 90° orientation provides a reference for ROI selection. In (b) histogram of ROI linear retardance and in (c) statistics on relevant polarization properties.

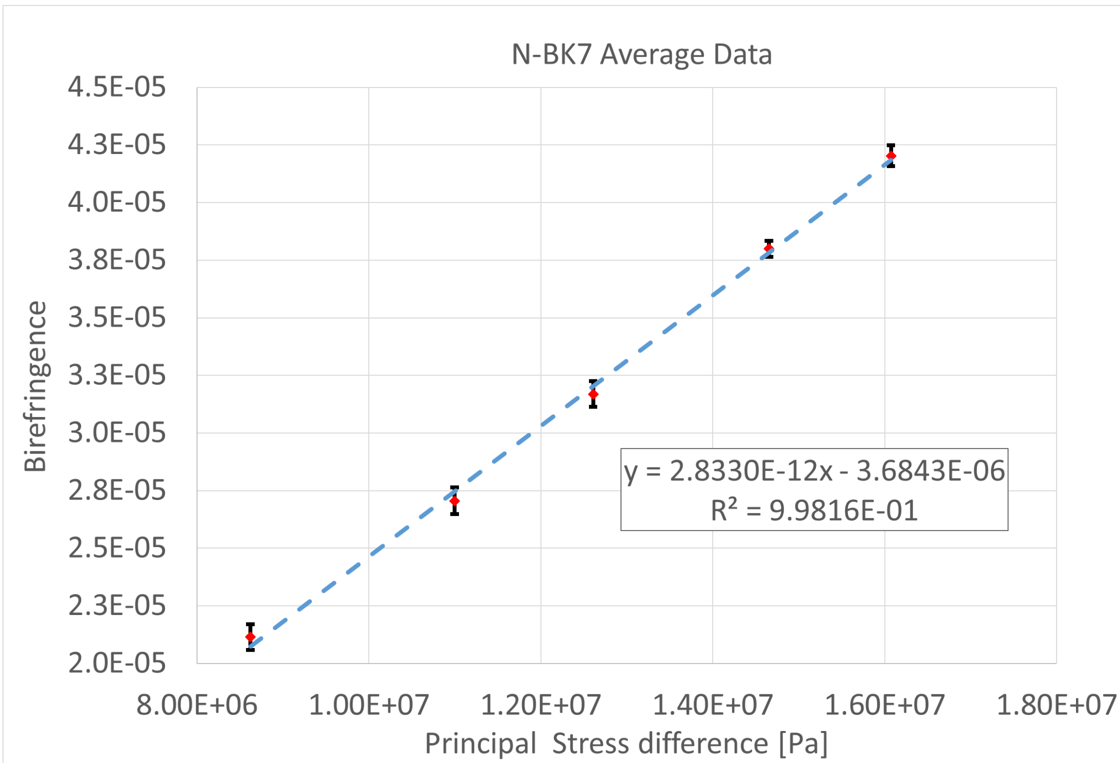

Figure 4.7 The measured birefringence versus principal stress difference for N-BK7 sample. Data is averaged over three independent trial runs. Linear fit gives a slope of $2.833 \pm 0.106[TPa]^{-1}$ which is within the reported value of $2.77[TPa]^{-1} \pm 3\%$[4]

APPENDIX A

IRCSP Electrical Design

The test flight which is hosting the IRCSP as a piggy back is only expected to last between 4 to 10 hours. The base instrument has minimal power consumption, modeled as 5 [W]. CSBF provides high-quality batteries capable of surviving the environmental conditions of high altitude which provide 30 Amp-hours at 30 Volts or 900 Watt-hours of power. The IRCSP is designed to operate from two of these battery packs connected in parallel providing 1800 Watt-hours at 30 Volts. At maximum cooling power and data collection rate, the instrument pulls 45 watts giving up to 40 hours of operation. The payload is controlled by an OTS Single Board Computer (SBC), (Ts7800v2-DWMI3 from technologic systems[46]) running a Linux/Debian9-Stretch operating system. The TS7800 was chosen due to its resilience to extreme temperatures ($-60[^{\circ}C]$, $200[^{\circ}C]$). A micro-controller reads out temperature, pressure, and humidity from numerous sensors placed internal and external to the IRCSP enclosure. The TEC is controlled through an OTS TEC control board based on a PID loop.

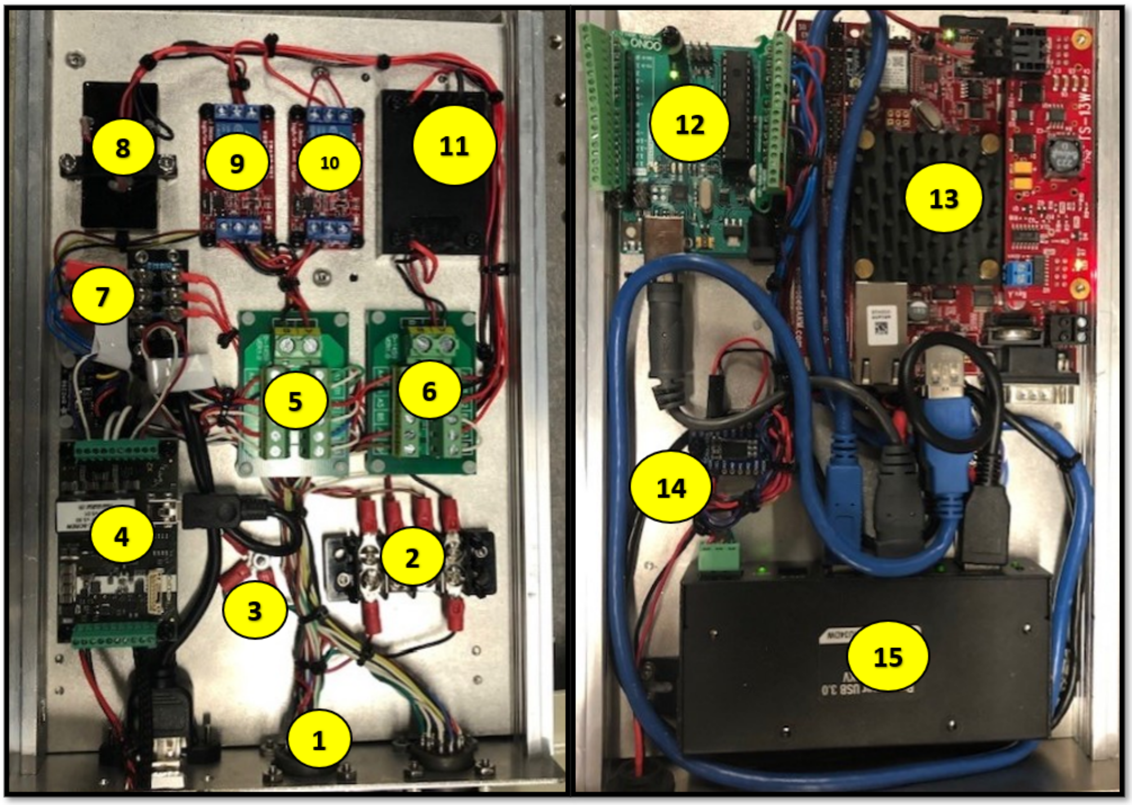

Figure A.1 Electronics enclosure of the IRCSP payload with components labelled. (1) Connector bulkhead to instrument (2) +30V battery distribution (3) Chassis ground (4) PID-loop TEC Controller (5) 12V distribution terminal (6) 5V distribution terminal (7) Thermistor reference resistors (8) 5V DC-DC converter (9) Context heater relay (10) lens heater relay (11) 12V DC-DC converter (12) Arduino Micro-controller (13) TS-7800-V2-DMW3I single-board computer (14) Multiplexer for BME280 sensors (15) powered USB hub.

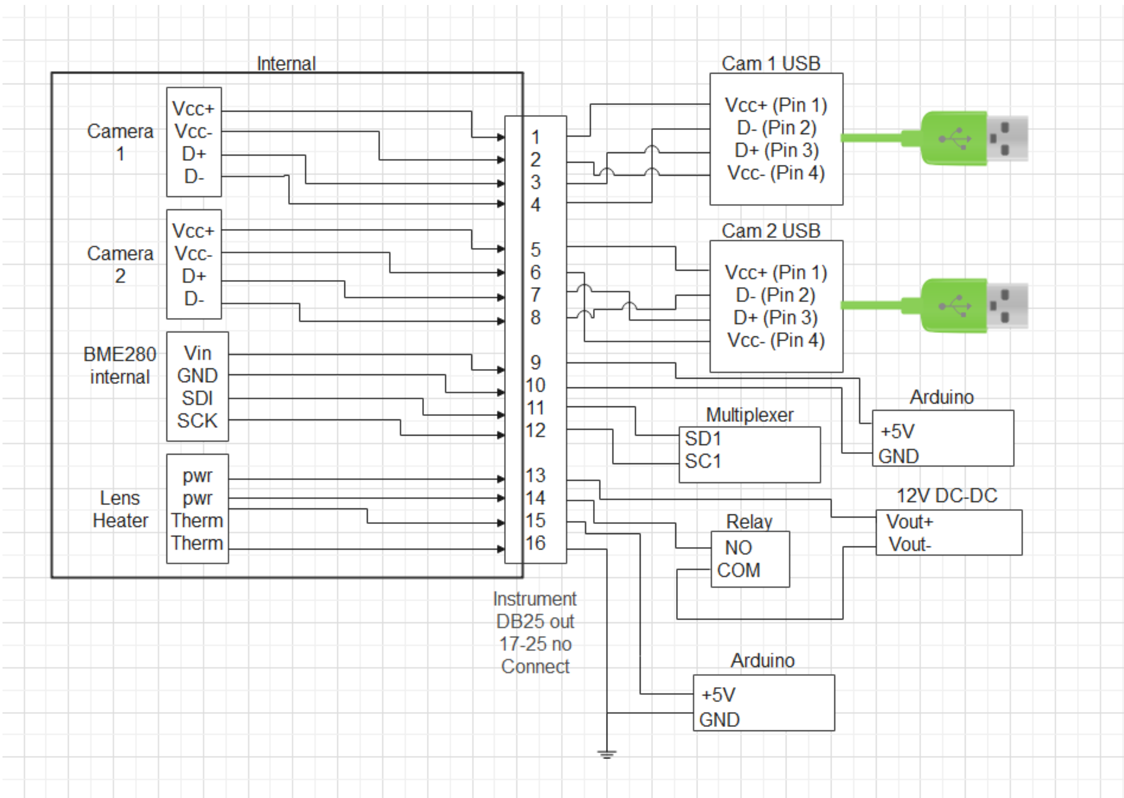

Figure A.2 Electrical schematic for wiring the DB25 connector connector for internal components.

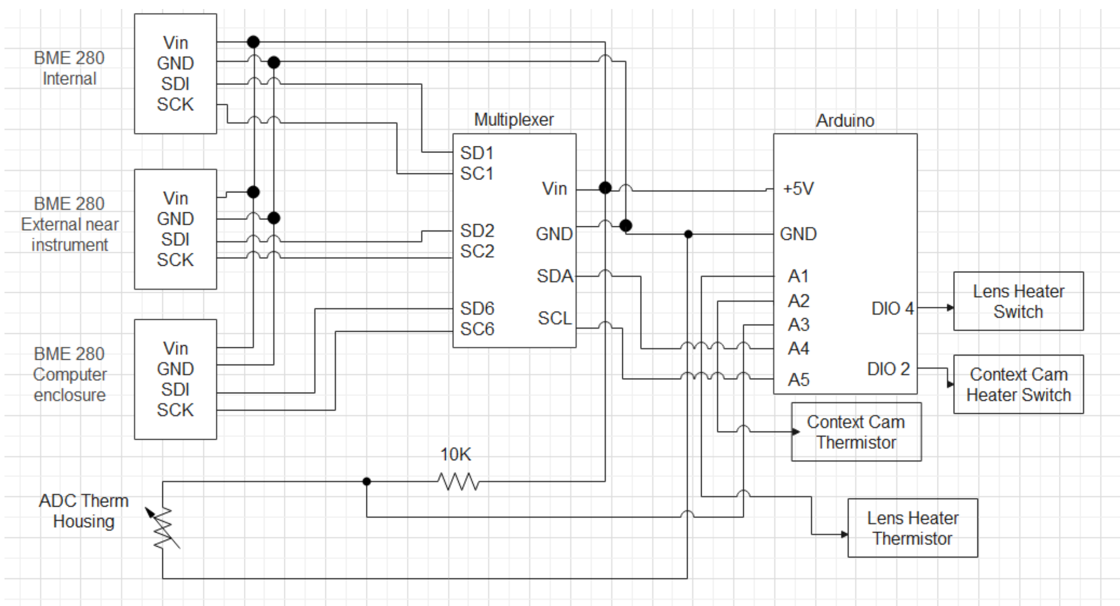

Figure A.3 Electrical schematic for the telemetry sensors on board the IRCSP.

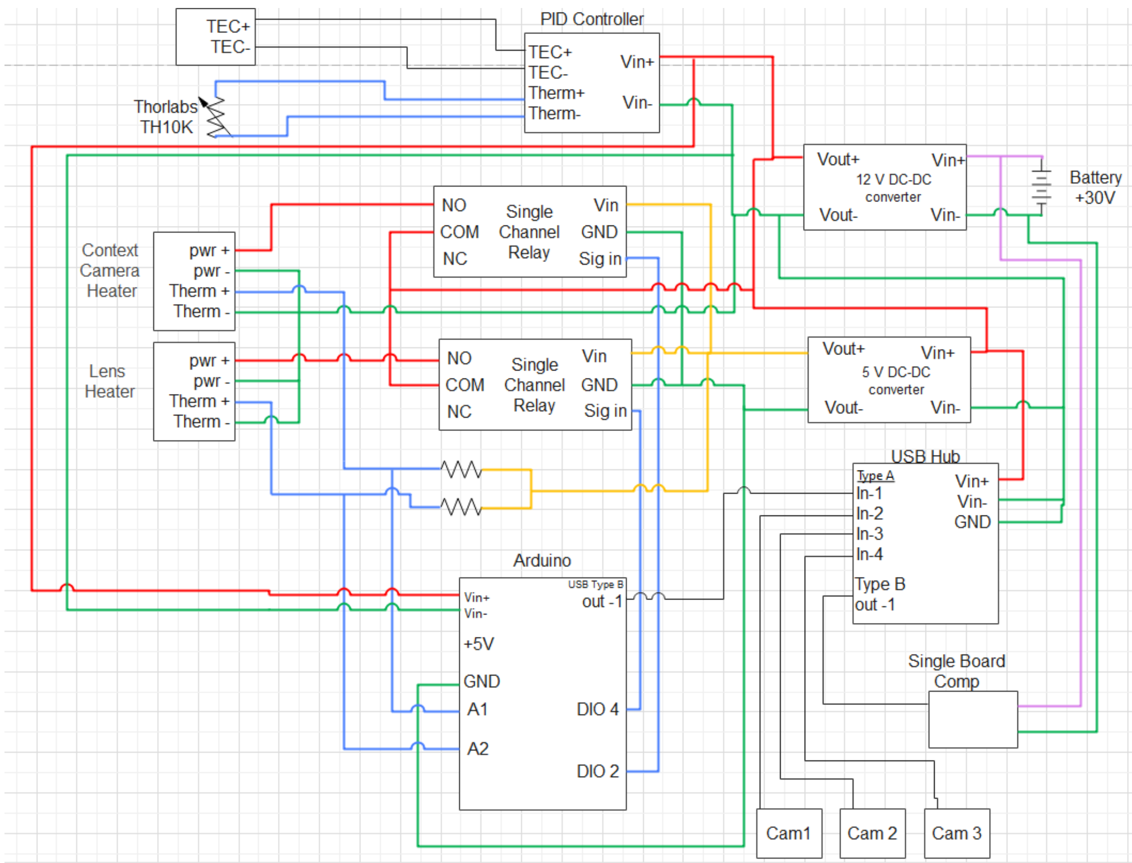

Figure A.4 Electrical schematic for on board heater circuits, thermistor sensors, and switches for triggering heating elements.

REFERENCES

[1] Wikipedia stress-strain curve. https://en.wikipedia.org/wiki/Stress-strain-curve. Accessed: 08/02/2023.

[2] Goddard Space Flight Center. 540-pg-8072.1.2b mechanical fastener torque guidelines. https://www.csbf.nasa.gov/documents/540-PG-8072.1.2, 2020.

[3] Wikipedia US standard atmosphere. https://en.wikipedia.org/wiki/U.S.-Standard-Atmosphere. Accessed: 08/02/2023.

[4] Schott Glass. Tie-27: Stress in optical glass. https://www.us.schott.com/shop/medias/schott-tie-27-stress-in-optical-glass-eng.pdf, 2004. Accessed: 05.24.2023.

[5] Goddard Space Flight Center. 820-pg-8700.0.1 gondola structural design requirements. https://www.csbf.nasa.gov/documents/gondola/820-PG-8700.0.1, 2019.

[6] American Institute of Aeronautics and Astronautics. Standard: Space systems—metallic pressure vessels, pressurized structures, and pressure components (ANSI/AIAA S-080A-2018), 2018.

[7] D. Wu, M. Vega, M. Solly, V. Marrero, K. Hart, S. Guerrero, W. Gaines, C. Du Toit, G. De Amici, W. Deal, A. Dabrowski, M. Coon, and R. Chipman. Swirp (submm-wave and long wave infrared polarimeter); a new tool for investigations of ice distribution and size in cyrrus clouds. In *IGARSS 2019 - 2019 IEEE International Geoscience and Remote Sensing Symposium*, pages 8436–8439, 2019.

[8] Kira A. Hart, Russell A. Chipman, and Dong L. Wu. Compact LWIR polarimeter for cirrus ice properties. In David B. Chenault and Dennis H. Goldstein, editors, *Polarization: Measurement, Analysis, and Remote Sensing XIII*, volume 10655, page 106550V. International Society for Optics and Photonics, SPIE, 2018.

[9] Kira A. Hart, Meredith K. Kupinski, Dong L. Wu, and Russell A. Chipman. First results from an uncooled LWIR polarimeter for cubesat deployment. *Optical Engineering*, 59(7):075103, 2020.

[10] Kira A. Hart Shanks, Russell A. Chipman, Jaclyn A. John, Jeremy C. Parkinson, Dong L. Wu, and Meredith K. Kupinski. Near space demonstration of a

compact LWIR spectro-polarimeter for ice cloud measurements. In David B. Chenault and Meredith K. Kupinski, editors, *Polarization: Measurement, Analysis, and Remote Sensing XV*, volume 12112, page 121120L. International Society for Optics and Photonics, SPIE, 2022.

[11] Kira Ann Shanks. *Infrared Polarimetry for Remote Sensing.* PhD thesis, The University of Arizona, 2022.

[12] Schott Glass. Data sheet, Schott N-BK7. https://www.schott.com/shop/medias/schott-datasheet-n-bk7-eng.pdf. Accessed: 05.24.2023.

[13] D. Vukobratovich and P. Yoder. *Fundamentals of Optomechanics.* Optical Sciences and Applications of Light. CRC Press, 2018.

[14] Russell A Chipman, Wai-Sze Tiffany Lam, and Garam Young. *Polarized light and optical systems.* CRC press, 2018.

[15] P. Yoder and D. Vukobratovich. *Opto-Mechanical Systems Design, Fourth Edition, Two Volume Set.* Taylor & Francis, 2015.

[16] Beer, Johnston, and E. Russell Johnston. *Mechanics of materials.* McGraw-Hill, New York, 1981.

[17] W.C. Young and R.G. Budynas. *Roark's Formulas for Stress and Strain.* MacGraw-Hill international edition. McGraw Hill LLC, 2001.

[18] J Jaap Wijker. *Spacecraft structures.* Springer Science & Business Media, 2008.

[19] American Institute of Aeronautics and Astronautics. Standard: Space systems—structures, structural components, and structural assemblies (aiaa s-110-2005), 2005.

[20] Hans Mueller. Theory of Photoelasticity in Amorphous Solids. *Physics*, 6(6):179–184, 06 1935.

[21] Hans Mueller. The theory of photoelasticity. *Journal of the American Ceramic Society*, 21(1):27–33, 1938.

[22] Robert C. Sampson. A stress-optic law for photoelastic analysis of orthotropic composites. *Experimental Mechanics*, 10:210–215, 1970.

[23] Keith B. Doyle and William M. Bell. Thermo-elastic wavefront and polarization error analysis of a telecommunication optical circulator. In *Current Developments in Lens Design and Optical Systems Engineering*, volume 4093, pages 18 – 27. International Society for Optics and Photonics, SPIE, 2000.

[24] P.S. Theocaris and E.E. Gdoutos. *Matrix Theory of Photoelasticity*. Springer series in optical sciences. Springer-Verlag, 1979.

[25] Raymond D Mindlin. A review of the photoelastic method of stress analysis. i. *Journal of Applied Physics*, 10(4):222–241, 1939.

[26] Amber Michelle Beckley. *Polarimetry and beam apodization using stress-engineered optical elements*. University of Rochester, 2012.

[27] US Standard Atmosphere. National oceanic and atmospheric administration. *National Aeronautics and Space Administration, United States Air Force, Washington, DC*, 1976.

[28] NASA Earth Atmosphere Model. https://www.grc.nasa.gov/www/k-12/airplane/atmosmet.html. Accessed: 2023-24-03.

[29] Uncooled, Longwave Infrared (LWIR) OEM Thermal Camera Module. https://www.flir.com/products/boson/?vertical=lwir&segment=oem. Accessed: 2023-24-07.

[30] Edmund K. Gyasi. *Enhancement of Thermal Management in Air Cooled Systems Operating at Low-Pressure Conditions*. PhD thesis, 2016. Copyright - Database copyright ProQuest LLC; ProQuest does not claim copyright in the individual underlying works; Last updated - 2023-03-04.

[31] Stuart W Churchil. Free convection around immersed bodies. *Heat exchanger design handbook*, 2, 2002.

[32] R. Hosseini and Maysam Saidi. Experimental study of air pressure effects on natural convection from a horizontal cylinder. *Heat Transfer Engineering*, 33:878–884, 01 2012.

[33] NASA Air Viscosity. https://www.grc.nasa.gov/www/k-12/airplane/viscosity.html. Accessed: 2023-24-03.

[34] Evan M Racine. Experimental study high altitude forced convective cooling of electromechanical actuation systems. Technical report, University of Dayton Research Institute Dayton United States, 2016.

[35] R.M Wilkinson, R Briet, C Ashman, G Sarri, B.G Jones, and C.I Jewell. A mechanical cooler for the spectrometer experiment on board the integral spacecraft1revised version of a presentation at the "1998 space cryogenics workshop, estec, noordwijk, netherlands, july 20–21 1998".1. *Cryogenics*, 39(2):179–183, 1999.

[36] H. Cease et al. Cooling the Dark Energy Camera CCD Array using a Closed-Loop, Two-Phase Liquid Nitrogen system. 7 2010.

[37] Liquid Cryogen Dewars. https://www.irlabs.com/products/cryostats/liquid-cryogen-dewars/. Accessed: 2023-24-07.

[38] Bruce Yost, Sasha Weston, Gabriel Benavides, Frederic Krage, John Hines, Stephanie Mauro, Selasi Etchey, Kiara O'Neill, and Barbra Braun. State-of-the-art small spacecraft technology. 2021.

[39] Alessandro Freddi, Giorgio Olmi, and Luca Cristofolini. Experimental stress analysis for materials and structures. *Stress analysis models for developing design methodologies. Series in solid and structural mechanics*, 1, 2015.

[40] A Ch Yiannopoulos. A general formulation of stress distribution in cylinders subjected to non-uniform external pressure. *Journal of Elasticity*, 56:181–198, 1999.

[41] K. Ramesh and K. Shins. Stress field equations for a disk subjected to self-equilibrated arbitrary loads: revisited. *Granular Matter*, 24(2):1434–7636, 2022.

[42] Jason T Gomez, Arun Shukla, and Atul Sharma. Photoelastic evaluation of stress fields and fracture during dynamic splitting experiments. *Journal of testing and evaluation*, 30(3):186–196, 2002.

[43] ASTM International. Astmc770-16r20 standard test method for measurement of glass stress—optical coefficient, 2020.

[44] J Scott Tyo. Design of optimal polarimeters: maximization of signal-to-noise ratio and minimization of systematic error. *Applied optics*, 41(4):619–630, 2002.

[45] R. M. A. Azzam. Photopolarimetric measurement of the Mueller matrix by fourier analysis of a single detected signal. *Optics Letters*, 2(6):148, Jun 1978.

[46] Technologic Systems, Inc. TS-7800-V2. https://www.embeddedts.com/products/TS-7800-V2. Accessed: 2023-16-08.